JPEDAV (2009) 30:351–366
DOI: 10.1007/s11669-009-9501-6
1547-7037 ©ASM International

Thermodynamic Assessment of the La-Fe-O System

E. Povoden-Karadeniz, A.N. Grundy, M. Chen, T. Ivas, and L.J. Gauckler

(Submitted December 17, 2007; in revised form February 11, 2009)

The La-Fe and the La-Fe-O systems are assessed using the Calphad approach, and the Gibbs energy functions of ternary oxides are presented. Oxygen and mutual La and Fe solubilities in body-centered cubic (bcc) and face-centered cubic (fcc) structured metallic phases are considered in the modeling. Oxygen nonstoichiometry of perovskite-structured $La_{1\pm x}Fe_{1\pm y}O_{3-\delta}$ is modeled using the compound energy formalism (CEF), and the model is submitted to a defect chemistry analysis. The contribution to the Gibbs energy of $LaFeO_3$ due to a magnetic order-disorder transition is included in the model description. Lanthanum-doped hexaferrite, $LaFe_{12}O_{19}$, is modeled as a stoichiometric phase. $\Delta_{f,elements}{}^{\circ}H_{298\ K}$ ($LaFe_{12}O_{19}$) = −5745 kJ/mol, ${}^{\circ}S_{298\ K}$ ($LaFe_{12}O_{19}$) = 683 J/mol · K, and $\Delta_{f,oxides}{}^{\circ}G$ ($LaFe_{12}O_{19}$) = 4634 − 37.071*T* (J/mol) from 1073 to 1723 K are calculated. The liquid phase is modeled using the two-sublattice model for ionic liquids. The calculated La-Fe phase diagram, $LaO_{1.5}$-FeO_x phase diagrams at different oxygen partial pressures, and phase equilibria of the La-Fe-O system at 873, 1073, and 1273 K as a function of oxygen partial pressures are presented.

Keywords defect chemistry, $LaFeO_3$, $LaFe_{12}O_{19}$, oxygen-solubility, perovskite, SOFC

1. Introduction

In solid oxide fuel cells (SOFCs) the thermodynamic stability of the cathode is particularly important for efficient long-term operation. Sr- and Co-doped lanthanum ferrites with the perovskite structure (LSCF) are used as cathode materials in SOFC. A thermodynamic database of the La-Sr-Fe-Co-O system is required for predictions of the stability of LSCF cathodes at SOFC operating temperatures and oxygen partial pressures. When using the Calphad approach for this purpose, one has to base the assessment of this quinary system on the model descriptions of the lower-order subsystems. In this paper the assessment of the La-Fe-O subsystem is presented. The La-Fe system comprises metallic double hexagonal close-packed (dhcp)-structured αLa, face-centered cubic (fcc)- and body-centered cubic (bcc)-structured La- and Fe-rich phases with small mutual solubilities of Fe and La, denoted as βLa_{ss}, γLa_{ss}, γFe_{ss}, αLa_{ss}, and δLa_{ss}. Small additions (∼0.042 to 0.6 at.%) of rare earth metals refine the structure of iron and steel considerably, and lead to higher strength, ductility, and enhanced hardness and durability.[1,2] Lanthanum further contributes to a high oxidation resistance of steel in dry and wet air.[3] This effect depends on the amount of oxygen dissolved in the steel: If the oxygen content is too high, lanthanum oxide will form, and the benefits of the lanthanum additive are lost. Modeling of the oxygen solubility in steel allows predictions under which conditions lanthanum oxide will form as an equilibrium phase. Hence, the modeling of the oxygen solubility in La-Fe metals is significant for steel research.

Ternary phases existing in the La-Fe-O system are perovskite-structured lanthanum ferrite, $La_{1\pm x}Fe_{1\pm y}O_{3-\delta}$ (prv) and hexagonal $LaFe_{12}O_{19}$ (hex). Doped hexaferrites are significant for industrial applications because of their magnetic anisotropy.[4] They reveal a complex layered structure, with Fe occurring on five different sites[5] and pure anionic layers intercalating with mixed anionic-cationic layers.[6]

2. Literature Review

2.1 La-Fe

A phase diagram of the La-Fe system based on available phase diagram data[7-10] is shown in Fig. 1 (dashed lines and symbols). The La-Fe phase diagrams in reviews from Gschneidner[7] and Spedding and Daane[8] are based on experimental work by Haefling and Daane that is not published elsewhere.

2.1.1 Solid Metals. General agreement between most researchers exists concerning the nonexistence of intermetallic phases at atmospheric pressure.[9,11,12] Only one author indicated peritectically melting $LaFe_2$ and $LaFe_5$ phases without giving experimental details or structural data,[13] but withdrew this again later.[14] The $\alpha Fe_{ss} \leftrightarrow \gamma Fe_{ss}$ transition temperature of La-saturated Fe is reduced by 6 K, and the transition temperature of $\gamma Fe_{ss} \leftrightarrow \delta Fe_{ss}$ is increased by 12 K compared to the pure Fe system.[15] No reasons

E. Povoden-Karadeniz, T. Ivas, and **L.J. Gauckler**, Department of Nonmetallic Inorganic Materials, ETH Zurich, Zurich, Switzerland; **A.N. Grundy**, Metallurgy and Process Organization, Concast AG, Zurich, Switzerland; **M. Chen**, Fuel Cells and Solid State Chemistry Department, Risoe National Laboratory, Technical University of Denmark, Lyngby, Denmark. Contact e-mail: erwin.povoden-karadeniz@tuwien.ac.at.

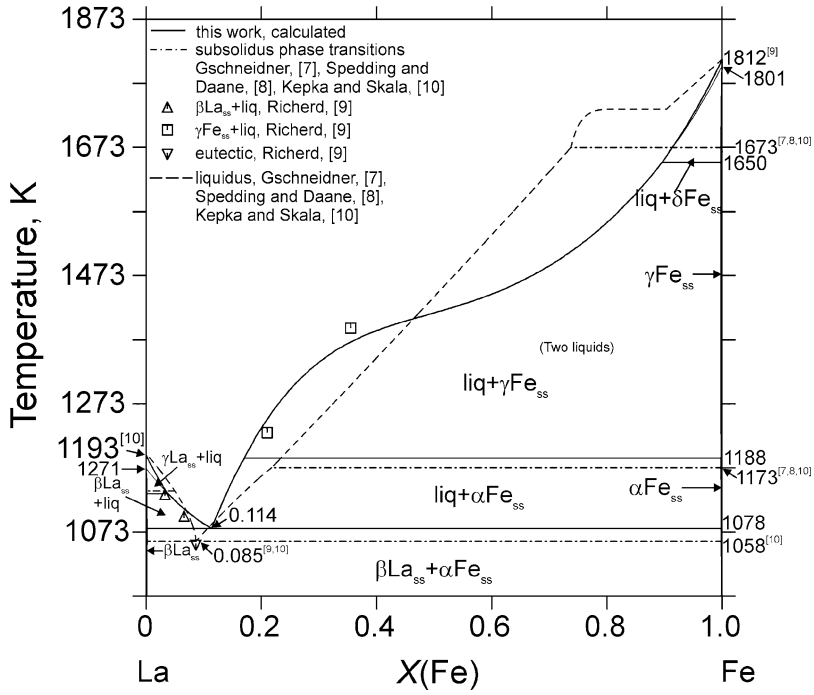

Fig. 1 Calculated phase diagram (solid lines) of the La-Fe system with data from the literature included (symbols, dashed, and dashed-dotted lines)

were given for the absence of γLa_{ss} and δFe_{ss} in the phase diagram of Richerd.[9] The maximum solubility of La in αFe_{ss} is: <0.1 at.% at 1053 K and <0.2 at.% at $\sim$1160 K.[8,10] Richerd[9] reported a maximum solubility of La in αFe_{ss} between 0.034 and 0.036 at.% at 873 K using microscopic and microprobe analysis of Fe with varying amounts of La impurities. This author states that the solubility of La in γFe_{ss} at 1203 K is not significantly higher than the solubility of La in αFe_{ss}. Savitskii[13] documented a larger solubility of La in αFe_{ss} and γFe_{ss}, but later[14] the same authors adopted the solubility values from Spedding and Daane.[8] The maximum solubility of Fe in βLa_{ss} is reported to be <0.25 at.% at $\sim$1053 K.[5,7,11] Richerd[9] quoted a Fe content of 0.25 at.% in βLa_{ss} at the solidus temperature of 1153 K.

2.1.2 Liquid Phase. Richerd[9] determined liquidus and eutectic temperatures and compositions using thermal analysis. Kepka and Skala[10] confirmed these earlier findings. Berezutskii et al.[16] and Esin et al.[17] determined enthalpies of mixing in La-Fe liquid from 0 to 35 at.% Fe at 1723 K and from 60 to 100 at.% Fe at 1923 K using high-temperature calorimetry.

The La-Fe system has a eutectic at 1053 ± 5 K[9] or 1058 K[10] and 8.5 at.% Fe.[9,10] Experimental liquidus data[9] indicate positive deviations from ideality. The flat liquidus between $\sim$80 and 92 at.% Fe with a very unlikely kink[18] at 92 at.% Fe was proposed by Haefling and Daane (cited in Ref 7, 8) without giving details on the experimental technique used and was adopted by Kepka and Skala[10] and Savitskii.[13] Only in the study by Richerd[9] who proposed a liquidus without anomaly is the experimental route transparent. Though a liquid-liquid miscibility gap was not found experimentally, opposite viewpoints exist concerning the liquid-liquid miscibility: Gschneidner[7] proposed that the liquidus anomaly is not caused by the formation of two immiscible liquids, but he did not propose mechanisms leading to this flattening. Okamoto[19] is also in favor of the version without miscibility gap, arguing that the anomaly would be too close to pure Fe. On the other hand Zhang and Li[15] stated that immiscibility regions must exist above the flat liquidus lines.

2.2 La-Fe-O

2.2.1 $LaO_{1.5}$-FeO_x Phase Diagram. The experimentally established phase diagram of the $LaO_{1.5}$-FeO_x system in air[20,21] is shown in Fig. 2 (symbols and dashed lines). Moruzzi and Shafer[20] used microscopic metallographic techniques and XRD to determine phase equilibria in quenched La-Fe oxide mixtures obtained by solid-state reaction of the oxides and coprecipitation of the hydroxides. They applied a rod-melting technique for the determination of solidus temperatures, and the technique was explained in some detail.[20] They found rhombohedral r-$La_{1\pm x}Fe_{1\pm y}O_{3-\delta}$ to melt congruently at 2163 ± 30 K. In an earlier study Cassedanne and Forestier[21] using XRD examined La-Fe oxide mixtures synthesized by coprecipitation of the hydroxides equilibrated at 1173, 1273, and 1573 K for 24 h. The phase equilibria at 1273 and 1573 K coincide in both studies.[20,21] Cassedanne and Forestier[21] reported no changes of these phase equilibria in samples equilibrated at $T \leq 1173$ K.

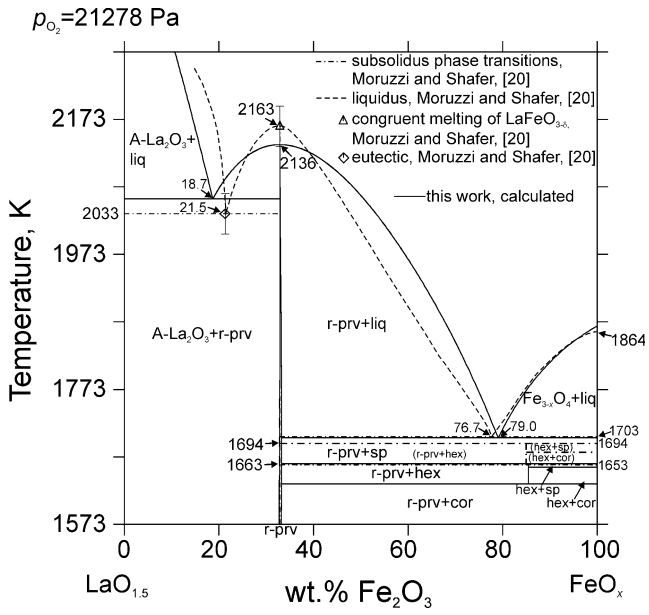

Fig. 2 Calculated $LaO_{1.5}$-FeO_x phase diagram in air (solid lines) with experimental phase diagram data included (symbols and broken lines). Error bars indicate the reported uncertainties of the experiments. Data of $LaFe_{12}O_{19}$ from Moruzzi and Shafer[20] written in brackets were not included in the optimization

2.2.2 Oxygen Solubility in Metals. Experimental oxygen solubilities in metallic Fe and La were considered in thermodynamic assessments by Kowalski and Spencer[22] and Grundy et al.[23]

2.2.3 Solid Oxides. In the perovskite phase, the thermodynamics of $La_{1\pm x}Fe_{1\pm y}O_{3-\delta}$ are well known from experimental investigations.[24-35] Data from these authors are listed in Table 1. Nakamura et al.[24] investigated the chemical stability of $La_{1\pm x}Fe_{1\pm y}O_{3-\delta}$ at 1273 K from pure oxygen to $p_{O_2} = 10^{-15}$ Pa using thermogravimetry combined with x-ray diffraction (XRD). Stølen et al.[25] determined the heat capacities of $LaFeO_3$ by adiabatic calorimetry from 13 to 900 K. Cheng and Navrotsky[26] determined the enthalpy of formation of $LaFeO_3$ by oxide melt solution calorimetry at 975 K. Tanasescu et al.[27] measured electromotive force (emf) of the solid oxide galvanic cell Pt/$LaFeO_3$, Fe, La_2O_3/7.44 at.% Y_2O_3-stabilized ZrO_2/FeO, Fe/Pt from 1073 to 1273 K, Sreedharan and Chandrasekharaiah[28] measured emf of Pt/$LaFeO_3$, Fe, La_2O_3/15 at.% CaO stabilized ZrO_2/FeO, Fe/Pt from 1094 to 1299 K, and Tretyakov et al.[29] measured emf of Pt/$LaFeO_3$, Fe, La_2O_3/Y_2O_3 stabilized ZrO_2/Pt, air atmosphere; the emf values were given for the temperature range from 1223 to 1473 K. Parida et al.[30] measured emf of Pt/$LaFeO_3$, Fe, La_2O_3/15 at.% CaO stabilized ZrO_2/NiO, Ni/Pt from 969 to 1234 K, and enthalpy increments of $LaFeO_3$ from 307.2 to 1000.0 K using a high-temperature Calvet microcalorimeter. Katsura et al.[31] and Kimizuka and Katsura[33] investigated isothermal phase equilibria of quenched La-Fe-oxide mixtures at varying oxygen partial pressures using XRD. Leontev et al.[34] measured the oxygen partial pressure of the decomposition of lanthanum ferrite to Fe and La_2O_3 at 1173, 1273, 1373, and 1473 K. Mizusaki et al.[35] ascribed the erratic fluctuations of their isothermal conductivity measurements of single phase lanthanum ferrite under low oxygen partial pressures to the decomposition of the perovskite phase.

$La_{1\pm x}Fe_{1\pm y}O_{3-\delta}$ is orthorhombic (o-prv) at temperatures up to 1278 ± 5 K, where it transforms to the rhombohedral structure (r-prv).[36] The enthalpy change of this transition was evaluated to be 350 ± 50 J/mol by Fossdal et al.[36] using differential thermal analysis (DTA). This first-order transition has been observed by Geller and Raccah[37] at 1253 to 1260 K by high-temperature powder XRD and DTA. A magnetic order-disorder transition was documented by Stølen et al.[25] to occur at $T \approx 735$ K. The defect chemistry of $La_{1\pm x}Fe_{1\pm y}O_{3-\delta}$ was investigated by Mizusaki et al.[35,38] based on thermogravimetric measurements of oxygen nonstoichiometry in lanthanum ferrite. Waernhus et al.[39,40] proposed a defect model for $La_{1\pm x}Fe_{1\pm y}O_{3-\delta}$ based on isothermal electrical conductivity measurements at 1273 K from pure oxygen atmosphere to $p_{O_2} = 10^{-12}$ Pa.

In the hexaferrite phase, the stability of $LaFe_{12}O_{19}$ is restricted to a small temperature range: it forms by the reaction:

$$\text{r-LaFeO}_{3-\delta} + \frac{11}{2}\text{Fe}_2\text{O}_3 \rightarrow \text{LaFe}_{12}\text{O}_{19} + \frac{1+2\delta}{4}\text{O}_{2(g)} \uparrow \quad \text{(Eq 1)}$$

at $T = 1633$ K as reported by Küpferling et al.[4] who used the same technique as Moruzzi and Shafer,[20] or at $T = 1653$ K.[20] Neglecting small cation-nonstoichiometries in spinel and lanthanum ferrite, a simplified reaction can be formulated for its decomposition at $T = 1663$ K[4] or $T = 1694$ K.[20] It reads

$$\text{LaFe}_{12}\text{O}_{19} \rightarrow \frac{11}{3}\text{Fe}_3\text{O}_4 + \text{r-LaFeO}_{3-\delta} + \frac{4+3\delta}{6}\text{O}_{2(g)} \uparrow \quad \text{(Eq 2)}$$

2.2.4 Liquid Phase. In the $LaO_{1.5}$-FeO_x quasi-binary system in air, two eutectics were found at 21.5 wt.% Fe_2O_3 and $T = 2033 \pm 30$ K, and 76.7 wt.% Fe_2O_3 and $T = 1703$ K on either side of the congruently melting lanthanum ferrite.[20] Moruzzi and Shafer[20] pointed out uncertainties of their high-temperature results caused by limitations of the strip-furnace technique used.

3. Thermodynamic Modeling and Optimization

The assessment of the La-Fe-O system is based on the recently reassessed La-O[41] and the Fe-O subsystems.[42] The two-sublattice ionic liquid model $(Fe^{2+},Fe^{3+})_p(O^{2-},Va^{q-})_q$ is adopted from Taylor and Dinsdale[43] for the liquid description in the Fe-O system. The lattice stabilities of elements are adopted from Dinsdale.[44]

3.1 Modeling of Metal Phases

3.1.1 Oxygen Solubility. In the bcc phase, proper modeling of the solubility of oxygen in bcc metal (Me) with an interstitial element X has been discussed recently by

Table 1 Calculated and experimental thermodynamic and phase stability data of lanthanum ferrite

Standard enthalpy of formation of $LaFeO_3$

$\Delta_{f,\ elements}\ {}^{\circ}H^{LaFeO_3}_{298\ K} = -1368.2$ kJ/mol this work, calculated
$\Delta_{f,elements}\ {}^{\circ}H^{LaFeO_3}_{298\ K} = -1373.48 \pm 2.61$ kJ/mol calculated from drop solution calorimetry[26]
$\Delta_{f,elements}\ {}^{\circ}H^{LaFeO_3}_{298.15\ K} = -1334.7$ kJ/mol calculated from Calvet microcalorimetry[30]
$\Delta_{f,oxides}\ {}^{\circ}H^{LaFeO_3}_{298\ K} = -60.75$ kJ/mol this work, calculated
$\Delta_{f,oxides}\ {}^{\circ}H^{LaFeO_3}_{975\ K} = -62.35$ kJ/mol this work, calculated
$\Delta_{f,oxides}\ {}^{\circ}H^{LaFeO_3}_{975\ K} = -64.58 \pm 3.9$ kJ/mol drop solution calorimetry in $3Na_2O \times 4MoO_3$[26]
$\Delta_{f,oxides}\ {}^{\circ}H^{LaFeO_3}_{975\ K} = -64.60 \pm 3.9$ kJ/mol drop solution calorimetry in $2PbO \times B_2O_3$(a)[26]

Standard entropy of $LaFeO_3$

${}^{\circ}S^{LaFeO_3}_{298\ K} = 107$ J/mol · K this work, calculated
${}^{\circ}S^{LaFeO_3}_{298.15\ K} = 110.6$ J/mol · K adiabatic calorimetry[25]
${}^{\circ}S^{LaFeO_3}_{298.15\ K} = 128.9$ J/mol · K Calvet microcalorimetry[30]
${}^{\circ}S^{LaFeO_3}_{900\ K} = 249$ J/mol · K this work, calculated
${}^{\circ}S^{LaFeO_3}_{900\ K} = 252.59$ J/mol · K Calvet microcalorimetry[25]

Gibbs energies of reaction

$La_2O_3 + Fe + \frac{3}{4}O_{2(g)} \rightarrow LaFeO_3$
$T = 1273$ K $\Delta^{\circ}G = -307,364$ J/mol this work, calculated
$T = 1273$ K $\Delta^{\circ}G = -309,700$J/mol thermogravimetry[24]
$T = 1477$ K $\Delta^{\circ}G = -281,993$ J/mol this work, calculated
$T = 1477$ K $\Delta^{\circ}G = -287,841 \pm 1255$ J/mol(b) gas equilibrium[33]
$\Delta^{\circ}G = -466,683 + 124.78T$ this work, calculated, 298 − 173 K
$\Delta^{\circ}G = -449,822 \pm 2000 + (123.2 \pm 2)T$(b) emf, reference electrode Fe-FeO(c)[27]
$\Delta^{\circ}G = -419,795 + 86.98T \pm 1900$(b) emf, reference electrode Fe-FeO(c)[28]
$\Delta^{\circ}G = -460,003 \pm 7556 + (119.08 \pm 0.00532)T$(b) emf, reference electrode air[29]
$\Delta^{\circ}G = -412,613 + 76.67T$(b) emf, reference electrode Ni-NiO(d)[30]
(continued next column)
$\Delta^{\circ}G = -457,728 + 115.14T \pm 418$(b) gas equilibrium[31]
$\Delta^{\circ}G = -474,639 + 128.45T$(b)[32]
$\Delta^{\circ}G = -468,177 + 119.27T$(b) gas equilibrium[34]
$\Delta^{\circ}G = -499,275 + 136.38T$(b) electrical conductivity[35]
$\frac{1}{2}La_2O_3 + \frac{1}{2}Fe_2O_3 \rightarrow LaFeO_3$(e)
$T = 1273$ K $\Delta^{\circ}G = -60,625$ J/mol this work, calculated
$T = 1273$ K $\Delta^{\circ}G = -62,835$ J/mol gravimetry[24]
$T = 1477$ K $\Delta^{\circ}G = -60,267$ J/mol this work, calculated
$T = 1477$ K $\Delta^{\circ}G = -66,066$ J/mol gas equilibrium[33]
$\Delta^{\circ}G = -62,848 + 1.746T$ this work, calculated
$\Delta^{\circ}G = -46,391 + 0.21T$ emf, reference electrode Fe-FeO[27]
$\Delta^{\circ}G = -16,364 - 36.01T$ emf, reference electrode Fe-FeO[28]
$\Delta^{\circ}G = -56,572 - 3.91T$ emf, reference electrode air[29]
$\Delta^{\circ}G = -9182 - 46.32T$ emf, reference electrode Ni-NiO[30]
$\Delta^{\circ}G = -54,297 - 7.85T$ gas equilibrium[31]
$\Delta^{\circ}G = -71,208 + 4.46T$[32]
$\Delta^{\circ}G = -64,746 - 3.72T$ gas equilibrium[34]
$\Delta^{\circ}G = -95,844 + 13.39T$ electrical conductivity[35]
$\frac{1}{2}La_2O_3 + \frac{3}{2}FeO \rightarrow \frac{1}{2}Fe + LaFeO_3$
$\Delta^{\circ}G = -68,507 + 24.518T$ this work, calculated
$\Delta^{\circ}G = -22,919 - 11.32T \pm 340$ emf, reference electrode Fe-FeO (c)[28]

Phase equilibria

$La_{1\pm x}Fe_{1\pm y}O_{3-\delta} - Fe_{1-x}O - Fe_{3-x}O_4$ equilibrium
$T = 1477$ K $p_{O_2} = 10^{-4.12}$ Pa this work, calculated
$T = 1477$ K $p_{O_2} = 10^{-4.13}$ Pa gas equilibrium[33]
$La_{1\pm x}Fe_{1\pm y}O_{3-\delta} - \gamma Fe - Fe_{1-x}O$ equilibrium
$T = 1477$ K $p_{O_2} = 10^{-6.89}$ Pa this work, calculated
$T = 1477$ K $p_{O_2} = 10^{-6.93}$ Pa gas equilibrium[33]
$La_{1\pm x}Fe_{1\pm y}O_{3-\delta} - \gamma Fe - A$ - La_2O_3 equilibrium
$T = 1273$ K $p_{O_2} = 10^{-11.83}$ Pa this work, calculated
$T = 1273$ K $p_{O_2} = 10^{-11.95}$ Pa gravimetry[24]
$T = 1477$ K $p_{O_2} = 10^{-8.34}$ Pa this work, calculated
$T = 1477$ K $p_{O_2} = 10^{-8.58}$ Pa gas equilibrium[33]

(a) Used for optimization. (b) $\Delta^{\circ}G = \frac{3}{4} \cdot 2.303\ RT \log p_{O_2}$ assuming stoichiometric prv, La_2O_3 and Fe. (c) Calculated using $Fe + \frac{1}{2}O^{2-} \rightarrow FeO$ $\Delta^{\circ}G = -264,533 + 65.46872\ T$. (d) Calculated using $Ni + \frac{1}{2}O^{2-} \rightarrow NiO$ $\Delta^{\circ}G = -234,540 + 85.35672\ T$. (e) $\Delta^{\circ}G$ calculated from $La_2O_3 + Fe + O_{2(g)} \rightarrow LaFeO_3$, incorporating $Fe + \frac{3}{4}O^{2-} \rightarrow \frac{1}{2}Fe_2O_3$ $\Delta^{\circ}G = 403,341 - 122.99\ T$ for the oxidation of Fe to Fe_2O_3

Hallstedt et al.[45] In case there is information of the ordering of element X between different vacant positions in bcc described by $(Me)_1(Va)_1(Va)_1(Va)_1$ this is taken into account, otherwise the disordered model for interstitials in bcc, $(Me)_1(Va,X)_3$ is to be used. To the authors' best knowledge, data of the ordering of oxygen in iron and lanthanum are lacking. Hence, the bcc phase with mutual solubilities of La and Fe and solubility of oxygen is described by the simplified two-sublattice description $(La,Fe)(Va,O)_3$.

In the assessment of oxygen solubilities in metallic Fe(bcc)[22] the Gibbs energy polynomial for the FeO_3 end member was defined as:

$$ {}^{\circ}G_{(Fe)(O)_3} - H^{SER}_{Fe} - 3H^{SER}_{O} = {}^{\circ}G_{Fe(bcc)}{}^{[44]} + 6 \cdot \left(\frac{1}{2}\ {}^{\circ}G_{O_2}{}^{[44]} + RT \ln P \right) \quad \text{(Eq 3)} $$

This is not in line with the stoichiometry given by the model. The Gibbs energy of the end member $(Fe)(O)_3$ is properly defined by:

$$ {}^{\circ}G_{(Fe)(O)_3} - H^{SER}_{Fe} - 3H^{SER}_{O} = {}^{\circ}G_{Fe(bcc)}{}^{[44]} + 3 \cdot \frac{1}{2}\ {}^{\circ}G_{O_2}{}^{[44]} + A + BT \quad \text{(Eq 4)} $$

H_x^{SER} is the standard enthalpy of the stable state of element x at 298.15 K and 10^5 Pa.[44] The optimization of the adjustable parameters A and B using the PARROT module of the Thermocalc software[46] oxygen-solubility data from Hepworth et al.[47] and Swisher and Turkdogan[48] led to the stable FeO_3 end member at high oxygen partial pressures and low temperatures in the La-Fe-O system. This unphysical result was prevented by a large value for the end member ${}^\circ G_{Fe:O}$ (A equals zero), and modeling of the oxygen solubility with the temperature dependence of ${}^\circ G_{Fe:O}$, BT, and a negative regular interaction parameter ${}^\circ L_{Fe:O,Va}$.

Data on the oxygen-solubility in Fe obtained in early studies lack accuracy, most likely due to experimental problems and considerable amounts of oxidizable impurities[47] and were thus not used for the optimization.

The Gibbs energy of the end member $(La)(O)_3$ is defined by:

$$ {}^\circ G_{(La)(O)_3} - H_{Fe}^{SER} - 3H_O^{SER} = {}^\circ G_{La(bcc)}{}^{[44]} + 3 \cdot \frac{1}{2} {}^\circ G_{O_2}^{gas[44]} + A + BT \quad \text{(Eq 5)} $$

Optimization of A and BT with the oxygen solubilities proposed by Grundy et al.[23] led to stable LaO_3 in a wide temperature and oxygen partial pressure range in the La-Fe-O system. This problem was circumvented by using the same modeling strategy described previously for Fe(bcc).

For the fcc phase, as for the bcc phase, the proposed Gibbs energy polynomial of the fcc phase does not agree with the stoichiometries given by the model. The Gibbs energy of the compound $(Fe)(O)_1$ is correctly defined analogously to $(La)(O)_1$ in Grundy et al.[23] and $(Co)(O)_1$ in Chen et al.[49] by:

$$ {}^\circ G_{(Fe)(O)_1} - H_{Fe}^{SER} - H_O^{SER} = {}^\circ G_{Fe(fcc)}{}^{[44]} + \frac{1}{2} {}^\circ G_{O_2}^{gas[44]} + A + BT \quad \text{(Eq 6)} $$

Oxygen-solubility data from Swisher and Turkdogan[48] were used for the optimization of A and B.

The Gibbs energy of the compound $(La)(O)$ was adopted from Grundy et al.[23] Because of the lack of experimental data, the oxygen solubility in the La-Fe metallic phases was modeled as an ideal extension of the oxygen solubilities in pure La and Fe.

3.1.2 Mutual Solubilities of La and Fe. In order to account for the small mutual solubilities of La in αFe_{ss} and Fe in γLa_{ss} reported,[7-10] the zeroth-order, composition-independent interaction parameter[50] ${}^0L_{Fe,La:Va}^{bcc}$ was given a large positive value, taking into account a temperature dependence.

For the fcc phase with mutual solubilities of La and Fe, the same modeling strategy as for the bcc phase was used: The formula $(La,Fe)(Va,O)_1$ was chosen, and ${}^0L_{Fe,La:Va}^{bcc}$ was given a large temperature-dependent positive value.

3.2 Modeling of Solid Oxides

3.2.1 Perovskite Phase. In oxygen-deficient $La_{1\pm x}Fe_{1\pm y}O_{3-\delta}$, $Fe^{3+} \rightarrow Fe^{2+}$ reduction is considered to take place on the B-site of $(A)_{1\pm x}(B)_{1\pm y}(O)_{3-\delta}$ perovskite, and vacancies on the anionic sublattice are required for charge neutrality. In early studies from Nakamura et al.[24] and Tofield and Scott[51] no oxidation of $LaFeO_3$ at 1273 K and $p_{O_2} = 10^5$ Pa,[24] and at 873 K and $p_{O_2} = 1.3 \times 10^7$ Pa[51] were reported. More recently Mizusaki et al.[35] and Waernhus et al.[39,40] proposed that vacancies on the A-site of the perovskite phase form as a result of slight oxidation, contributing to its defect chemistry. It was also stated[39] that in addition oxygen on interstitial sites may compensate for the oxidation of Fe^{3+}. This contradicts a study from Tofield and Scott.[51] Their refinement of neutron diffraction analyses of $LaMnO_{3+\delta}$ indicate that a model description involving oxygen on interstitial sites is very unlikely. Small amounts of Fe^{4+} in single-phase $LaFeO_{3-\delta}$ synthesized at 923 K[52] and 1073 K[53] in air atmosphere were determined by chemical analysis[52] and temperature programmed reduction,[53] validating some oxidation of lanthanum ferrite. Both small La and Fe deficiencies in single-phase perovskite sintered at 1573 K were reported by Waernhus et al.[39] In order to account for the findings from Porta et al.,[52] Ciambelli et al.,[53] and Waernhus et al.[39] the sublattice model $(La^{3+},Va)(Fe^{2+},Fe^{3+},Fe^{4+},Va)(O^{2-},Va)_3$ was chosen to describe the nonstoichiometry of lanthanum ferrite. Using the compound energy formalism (CEF)[54-56] the molar Gibbs energy of $La_{1\pm x}Fe_{1\pm y}O_{3-\delta}$ then reads:

$$ {}^\circ G_m^{prv} = \sum_i \sum_j \sum_k y_i y_j y_k \, {}^\circ G_{i:j:k} + RT\left(\sum_i y_i \ln y_i + \sum_j y_j \ln y_j + 3\sum_k y_k \ln y_k\right) + G_{mag} + {}^E G_m^{prv} \quad \text{(Eq 7)} $$

where y_i is the site fraction of Va and La^{3+} on the A sublattice, y_j is the site fraction of Fe^{2+}, Fe^{3+}, Fe^{4+}, and Va on the B sublattice and y_k is the site fraction of O^{2-} and Va on the O sublattice of the perovskite $A_{1\pm x}B_{1\pm y}O_{3-\delta}$, and $R = 8.31451$ J/mol·K. The third-last term accounts for the configurational entropy of mixing. The second-last term stands for the magnetic contribution to the Gibbs energy. The last term describes the excess Gibbs energy of mixing; as we introduce no interaction parameter, it is equal to 0 in this work. The parameters of the compound energy formalism are the Gibbs energies of the 16 end-member compounds ${}^\circ G_{i:j:k}$ that are not necessarily neutral. The Gibbs energy function of stoichiometric orthorhombic $LaFeO_3$, ${}^\circ G_{LaFeO_3}^{o-prv}$ is given by:

$$ {}^\circ G_{LaFeO_3}^{o-prv} - H_{La}^{SER} - H_{Fe}^{SER} - 3H_O^{SER} = {}^\circ G_{La^{3+}:Fe^{3+}:O^{2-}} = \text{GPRV} = \frac{1}{2} {}^\circ G_{Fe_2O_3}{}^{[42]} + \frac{1}{2} {}^\circ G_{La_2O_3}{}^{[41]} + G_{mag} + A + B\text{T} + CT\ln T \quad \text{(Eq 8)} $$

The parameters A, B, and C are optimized using the enthalpy of formation from Cheng and Navrotsky,[26] heat capacity data from Stølen et al.,[25] enthalpy increment data from Parida et al.,[30] oxygen partial pressures of the $Fe\text{-}La_2O_3\text{-}La_{1\pm x}Fe_{1\pm y}O_{3-\delta}$ equilibrium from Nakamura et al.,[24] and emf data from Parida et al.,[30] Sreedharan and Chandrasekharaiah,[28] and Tretyakov et al.[29] below

the orthorhombic ↔ rhombohedral transition temperature. $A + BT$ parameters of the high-temperature rhombohedral perovskite phase, r-prv, were optimized using the transition temperature and the enthalpy of transition from Fossdal et al.,[36] and experimental data above the orthorhombic ↔ rhombohedral transition temperature: oxygen partial pressures of the Fe-La_2O_3-$La_{1\pm x}Fe_{1\pm y}O_{3-\delta}$ and $Fe_{1-x}O$-$Fe_{3-x}O_4$-$La_{1\pm x}Fe_{1\pm y}O_{3-\delta}$ equilibria from Katsura et al.[31] and Kimizuka and Katsura,[33] emf data from Sreedharan and Chandrasekharaiah[28] and Tretyakov et al.,[29] and oxygen nonstoichiometry data from Mizusaki et al.[38] The optimized Gibbs energy function of the neutral stoichiometric compound is denoted as GRPRV in Table 2.

The sublattice occupancy of the completely reduced perovskite reads $(La^{3+})(Fe^{2+})(O^{2-}_{5/6}Va_{1/6})_3$. Its Gibbs energy is given by:

$$\begin{aligned}&{}^{\circ}G^{\text{o-prv}}_{LaFeO_{2.5}} - H^{SER}_{La} - H^{SER}_{Fe} - 2.5H^{SER}_{O}\\&= \frac{5}{6}\,{}^{\circ}G_{La^{3+}:Fe^{2+}:O^{2-}} + \frac{1}{6}\,{}^{\circ}G_{La^{3+}:Fe^{2+}:Va} + 3RT\left(\frac{5}{6}\ln\frac{5}{6} + \frac{1}{6}\ln\frac{1}{6}\right)\\&= \text{GPRVRED} = {}^{\circ}G_{FeO}{}^{[42]} + \frac{1}{2}\,{}^{\circ}G_{La_2O_3}{}^{[41]} + G_{mag} + A\end{aligned} \quad \text{(Eq 9)}$$

The neutral oxidized end members read:

$$\begin{aligned}&{}^{\circ}G^{\text{o-prv}}_{LaFe_{0.75}O_3} - H^{SER}_{La} - 0.75H^{SER}_{Fe} - 3H^{SER}_{O}\\&= \frac{3}{4}\,{}^{\circ}G_{La^{3+}:Fe^{4+}:O^{2-}} + \frac{1}{4}\,{}^{\circ}G_{La^{3+}:Va:O^{2-}} + RT\left(\frac{3}{4}\ln\frac{3}{4} + \frac{1}{4}\ln\frac{1}{4}\right)\\&= \text{GPRVOX1} = \frac{3}{8}\,{}^{\circ}G_{Fe_2O_3}{}^{[42]} + \frac{1}{2}\,{}^{\circ}G_{La_2O_3}{}^{[41]} + \frac{3}{16}\,{}^{\circ}G^{gas[44]}_{O_2}\\&\quad + G_{mag} + A + BT\end{aligned} \quad \text{(Eq 10)}$$

and

$$\begin{aligned}&{}^{\circ}G^{\text{o-prv}}_{La_{2/3}FeO_3} - \frac{2}{3}H^{SER}_{La} - H^{SER}_{Fe} - 3H^{SER}_{O} = \frac{2}{3}\,{}^{\circ}G_{La^{3+}:Fe^{4+}:O^{2-}}\\&\quad + \frac{1}{3}\,{}^{\circ}G_{Va:Fe^{4+}:O^{2-}} + RT\left(\frac{2}{3}\ln\frac{2}{3} + \frac{1}{3}\ln\frac{1}{3}\right) = \text{GPRVOX2}\\&= \frac{1}{2}\,{}^{\circ}G_{Fe_2O_3}{}^{[42]} + \frac{1}{3}\,{}^{\circ}G_{La_2O_3}{}^{[41]} + \frac{1}{4}\,{}^{\circ}G^{gas[44]}_{O_2} + G_{mag} + A\end{aligned} \quad \text{(Eq 11)}$$

The configurational entropy term in Eq 9 describes random mixing of O^{2-} with Va on the anionic sublattice. In Eq 10 and 11, it describes random mixing of Fe^{4+} and Va and La^{3+} and Va, respectively, on the cationic sublattices.

The parameters ${}^{\circ}G_{La^{3+}:Va:O^{2-}}$, ${}^{\circ}G_{Va:Va:O^{2-}}$, ${}^{\circ}G_{La^{3+}:Va:Va}$, and ${}^{\circ}G_{Va:Va:Va}$ are taken from Grundy et al.[57] The remaining 12 °G parameters containing Fe are obtained using Eq 9 to 11 and nine reciprocal relations analogously to Grundy et al.[57] that were all given the reciprocal energy 0.

The parameters A and B in Eq 9 to 11 were optimized using oxygen nonstoichiometry data,[38] oxygen partial pressures of the Fe-La_2O_3-$La_{1\pm x}Fe_{1\pm y}O_{3-\delta}$ equilibrium,[24] and emf data[28-30] below the orthorhombic ↔ rhombohedral transition temperature. The Gibbs energy functions of the neutral oxidized end members (GRPRVOX1 and GRPRVOX2 in Table 2) were equated with GPRVOX1 and GPRVOX2. Optimization of $A + BT$ of the reduced end member of r-prv (GRPRVRED in Table 2) using experimental data above the orthorhombic ↔ rhombohedral transition temperature led to a better reproduction of the experiments.

For the magnetic part of the Gibbs energy a magnetic ordering model proposed by Inden[58] and simplified by Hillert and Jarl[59] was used. A short summary of this model can be found in Chen et al.[49] The magnetic parameters T_c and β were fitted to the C_P data around the magnetic transition temperature.

The defect chemistry analysis of $La_{1\pm x}Fe_{1\pm y}O_{3-\delta}$ was done analogously to Grundy et al.[60]

3.2.2 Hexaferrite Phase. The Gibbs energy function of $LaFe_{12}O_{19}$ with the simplified structural-chemical formula $(La^{3+})(Fe^{2+})(Fe^{3+})_{11}(O^{2-})_{19}$ according to Deschamps and Bertaut[61] was based on the sum of the Gibbs energy functions of La_2O_3, Fe_2O_3, and FeO in proper stoichiometries:

$$\begin{aligned}G\text{LaFe}_{12}\text{O}_{19} = {}&\frac{1}{2}G(\text{La}_2\text{O}_3)^{[41]} + \frac{11}{2}G(\text{Fe}_2\text{O}_3)^{[42]}\\&+ G(\text{FeO})^{[42]} + A + BT\end{aligned} \quad \text{(Eq 12)}$$

A and B were optimized using the most recently reported formation and decomposition temperatures of $LaFe_{12}O_{19}$.[4]

3.2.3 Liquid Phase. The two-sublattice model for ionic liquids[62,63] was used for the description of the liquid phase of the La-Fe-O system. It was based on the liquid descriptions of the binary subsystems. The iron species considered in the liquid are Fe^{2+} and Fe^{3+}. Higher oxidation states are unlikely to exist in the liquid at normal oxygen partial pressures. Two different models for the Fe-O liquid have been presented: $(Fe^{2+},Fe^{3+})_p(O^{2-},Va^{q-})_q$ was used by Taylor and Dinsdale,[43] whereas Selleby and Sundman[42] proposed the description $(Fe^{2+})_p(FeO_{3/2}, O^{2-},Va^{q-})_q$. Extending the latter model to the La-Fe-O system a large negative BT of ${}^{0}L^{liq}_{Fe^{2+}:FeO_{3/2}O^{2-}}$ is required to reproduce the experimental data properly. Thus the authors chose the model description $(La^{3+},Fe^{2+},Fe^{3+})_p(O^{2-},Va^{q-})_q$. ${}^{\circ}G^{liq}_{La^{3+}:Va^{q-}}$, ${}^{\circ}G^{liq}_{La^{3+}:O^{2-}}$, ${}^{\circ}G^{liq}_{Fe^{3+}:Va^{q-}}$, ${}^{\circ}G^{liq}_{Fe^{2+}:O^{2-}}$, ${}^{\circ}G^{liq}_{Fe^{2+}:Va^{q-}}$, ${}^{\circ}G^{liq}_{Fe^{3+}:O^{2-}}$, and interaction parameters $L^{liq}_{Fe^{2+}:O^{2-},Va^{q-}}$ and $L^{liq}_{Fe^{3+},Fe^{2+}:O^{2-}}$ were taken from Zinkevich et al.,[41] Dinsdale,[44] Selleby and Sundman,[42] and Taylor and Dinsdale.[43] ${}^{\circ}G^{liq}_{Fe^{3+}:Va^{q-}}$ is obtained by the reciprocal reaction:

$${}^{\circ}G^{liq}_{Fe^{3+}:Va^{q-}} + 3{}^{\circ}G^{liq}_{Fe^{2+}:O^{2-}} - 2{}^{\circ}G^{liq}_{Fe^{2+}:Va^{q-}} - {}^{\circ}G^{liq}_{Fe^{3+}:O^{2-}} = 0 \quad \text{(Eq 13)}$$

The experimentally determined temperature and liquid composition at the eutectic in the metallic La-Fe system,[9] liquidus compositions at different temperatures,[9] and selective partial enthalpies of mixing of iron, $\Delta\bar{H}_{Fe}$[16] and lanthanum, $\Delta\bar{H}_{La}$[17] in La-Fe liquid as well as integral enthalpies of mixing, ΔH[17] were used to optimize the temperature-dependent regular ${}^{0}L^{liq}_{Fe^{2+},La^{3+}:Va}$ and subregular ${}^{1}L^{liq}_{Fe^{2+},La^{3+}:Va}$ interaction parameters to account for interactions between La and Fe.

Table 2 Model descriptions and Gibbs energy functions of the La-Fe-O system

Liquid (liq)

$(La^{3+}, Fe^{2+}, Fe^{3+})_p(O^{2-}, Va^{q-})_q$

$p = 2y_{O^{2-}} + qy_{Va}, q = 3y_{La^{3+}} + 2y_{Fe^{2+}} + 3y_{Fe^{3+}}$

$^{\circ}G^{liq}_{La^{3+}:Va^{q-}} - H^{SER}_{La} = GLALIQ$[44]

$^{\circ}G^{liq}_{La^{3+}:O^{2-}} - 2H^{SER}_{La} - 3H^{SER}_{O} = GLA2O3LIQ$[41]

$^{\circ}G^{liq}_{Fe^{2+}:Va^{q-}} - H^{SER}_{Fe} = GFELIQ$[44]

$^{\circ}G^{liq}_{Fe^{3+}:Va^{q-}} - H^{SER}_{Fe} = 2GFELIQ$[44] $- GFEOLIQ$[43] $- 179,638 + 79.923T$

$^{\circ}G^{liq}_{Fe^{3+}:O^{2-}} - 2H^{SER}_{Fe} - 3H^{SER}_{O} = 5GFEOLIQ - 179,638 + 79.923T$[43]

$^{\circ}G^{liq}_{Fe^{2+}:O^{2-}} - 2H^{SER}_{Fe} - 2H^{SER}_{O} = 4GFEOLIQ$[43]

Interaction terms

$L^{liq}_{Fe^{2+}:O^{2-},Va^{q-}} = 176,681 - 16.368T + (-65,655 + 30.869T)(y_{O^{2-}} - y_{Va})$[43]

$L^{liq}_{Fe^{3+},Fe^{2+}:O^{2-}} = -26,362 + 13,353(y_{Fe^{3+}} - y_{Fe^{2+}})$[43]

$L^{liq}_{Fe^{2+},La^{3+}:Va^{q-}} = -41 + 15.2T + (-7837 + 4.9T)(y_{Fe^{2+}} - y_{La^{3+}})$

$L^{liq}_{Fe^{3+},La^{3+}:O^{2-}} = -136,242 + (-9285)(y_{Fe^{3+}} - y_{La^{3+}})$

$L^{liq}_{Fe^{2+},La^{3+}:O^{2-}} = -136,242 + (-9285)(y_{Fe^{2+}} - y_{La^{3+}})$

bcc A2 phase

$(La,Fe)(Va,O)_3$

$^{\circ}G^{bcc}_{Fe:Va} - H^{SER}_{Fe} = GHSERFE$[44]

$^{\circ}G^{bcc}_{La:Va} - H^{SER}_{La} = GLABCC$[44]

$^{\circ}G^{bcc}_{Fe:O} - H^{SER}_{Fe} - 3H^{SER}_{O} = GHSERFE + 3GHSEROO + 271.74T$

$^{\circ}G^{bcc}_{La:O} - H^{SER}_{La} - 3H^{SER}_{O} = GLABCC$[44] $+ 3GHSEROO + 35T$[44]

$L^{bcc}_{Fe,La:Va} = 30,358 + 23.67T$

$L^{bcc}_{Fe:O,Va} = -526,267.6$

$L^{bcc}_{La:O,Va} = -1,400,000$

$p = 0.4$[44]

$T^{bcc}_{c} = 1043y_{Fe}$[44]

$\beta^{bcc} = 2.22y_{Fe}$[44]

fcc A1 phase

$(La,Fe)(Va,O)$

$^{\circ}G^{fcc}_{Fe:Va} - H^{SER}_{Fe} = GFEFCC$[44]

$^{\circ}G^{fcc}_{La:Va} - H^{SER}_{La} = GLAFCC$[44]

$^{\circ}G^{fcc}_{Fe:O} - H^{SER}_{Fe} - H^{SER}_{O} = GFEFCC + GHSEROO - 175,707 + 88.23T$[44]

$^{\circ}G^{fcc}_{La:O} - H^{SER}_{La} - H^{SER}_{O} = GLAFCC + GHSEROO - 570,000 + 91.47T$[23]

$L^{fcc}_{Fe,La:Va} = 35,052 + 22.45T$

$p = 0.28$

$T^{fcc}_{c} = -201y_{Fe}$[44]

$\beta^{fcc} = -2.1y_{Fe}$[44]

$La_{1\pm x}Fe_{1\pm y}O_{3-\delta}$ perovskite

$(La^{3+}, Va)(Fe^{4+}, Fe^{3+}, Fe^{2+}, Va)(O^{2-}, Va)_3$

Orthorhombic perovskite, o-prv

$^{\circ}G^{o-prv}_{La^{3+}:Fe^{3+}:O^{2-}} - H^{SER}_{La} - H^{SER}_{Fe} - 3H^{SER}_{O} = GPRV$

$^{\circ}G^{o-prv}_{La^{3+}:Fe^{3+}:Va} - H^{SER}_{La} - H^{SER}_{Fe} = GPRV - 3GHSEROO$

$^{\circ}G^{o-prv}_{La^{3+}Fe^{2+}:O^{2-}} - H^{SER}_{La} - H^{SER}_{Fe} - 3H^{SER}_{O} = GPRVRED + 0.5GHSEROO + 11.2386T$

$^{\circ}G^{o-prv}_{La^{3+}:Fe^{2+}:Va} - H^{SER}_{La} - H^{SER}_{Fe} = GPRVRED - 2.5GHSEROO + 11.2386T$

$^{\circ}G^{o-prv}_{Va:Fe^{2+}:O^{2-}} - H^{SER}_{Fe} - 3H^{SER}_{O} = GPRVRED + 1.5GPRVOX2 + 0.5GVVV - 2GPRVOX1 + 2GHSEROO + 9.82596T$

$^{\circ}G^{o-prv}_{Va:Fe^{2+}:Va} - H^{SER}_{Fe} = GPRVRED + 1.5GPRVOX2 + 0.5GVVV - 2GPRVOX1 - GHSEROO + 9.82596T$

$^{\circ}G^{o-prv}_{Va:Fe^{3+}:O^{2-}} - H^{SER}_{Fe} - 3H^{SER}_{O} = GPRV + 1.5GPRVOX2 + 0.5GVVV - 2GPRVOX1 + 1.5GHSEROO - 1.41263T$

$^{\circ}G^{o-prv}_{Va:Fe^{3+}:Va} - H^{SER}_{Fe} = GPRV + 1.5GPRVOX2 + 0.5GVVV - 2GPRVOX1 - 1.5GHSEROO - 1.41263T$

Rhombohedral perovskite (r-prv)

$^{\circ}G^{r-prv}_{La^{3+}:Fe^{3+}:O^{2-}} - H^{SER}_{La} - H^{SER}_{Fe} - 3H^{SER}_{O} = GRPRV$

$^{\circ}G^{r-prv}_{La^{3+}:Fe^{3+}:Va} - H^{SER}_{La} - H^{SER}_{Fe} = GRPRV - 3GHSEROO$

(continued next column)

$^{\circ}G^{r-prv}_{La^{3+}:Fe^{2+}:O^{2-}} - H^{SER}_{La} - H^{SER}_{Fe} - 3H^{SER}_{O} = GRPRVRED + 0.5GHSEROO + 11.2386T$

$^{\circ}G^{r-prv}_{La^{3+}:Fe^{2+}:Va} - H^{SER}_{La} - H^{SER}_{Fe} = GRPRVRED - 2.5GHSEROO + 11.2386T$

$^{\circ}G^{r-prv}_{Va:Fe^{2+}:O^{2-}} - H^{SER}_{Fe} - 3H^{SER}_{O} = GRPRVRED + 1.5GPRVOX2 + 0.5GVVV - 2GPRVOX1 + 2GHSEROO + 9.82596T$

$^{\circ}G^{r-prv}_{Va:Fe^{2+}:Va} - H^{SER}_{Fe} = GRPRVRED + 1.5GPRVOX2 + 0.5GVVV - 2GPRVOX1 - GHSEROO + 9.82596T$

$^{\circ}G^{r-prv}_{Va:Fe^{3+}:O^{2-}} - H^{SER}_{Fe} - 3H^{SER}_{O} = GRPRV + 1.5GPRVOX2 + 0.5GVVV - 2GPRVOX1 + 1.5GHSEROO - 1.41263T$

$^{\circ}G^{r-prv}_{Va:Fe^{3+}:Va} - H^{SER}_{Fe} = GRPRV + 1.5GPRVOX2 + 0.5GVVV - 2GPRVOX1 - 1.5GHSEROO - 1.41263T$

Orthorhombic and rhombohedral perovskite

$^{\circ}G^{prv}_{La^{3+}:Fe^{4+}:Va} - H^{SER}_{La} - H^{SER}_{Fe} = 2/3GPRVOX1 + 0.5GPRVOX2 - 1/6GVVV - 3.5GHSEROO + 5.76318T$

$^{\circ}G^{prv}_{La^{3+}:Va:O^{2-}} - H^{SER}_{La} - 3H^{SER}_{O} = 2GL4VO - 1.5GLV4O + 0.5GVVV + 1.5GHSEROO + 1.41263T$

$^{\circ}G^{prv}_{La^{3+}:Va:Va} - H^{SER}_{La} = 2GL4VO - 1.5GLV4O + 0.5GVVV - 1.5GHSEROO + 1.41263T$

$^{\circ}G^{prv}_{La^{3+}:Fe^{4+}:O^{2-}} - H^{SER}_{La} - H^{SER}_{Fe} - 3H^{SER}_{O} = 2/3GPRVOX1 + 0.5GPRVOX2 - 1/6GVVV - 0.5GHSEROO + 5.76318T$

$^{\circ}G^{prv}_{Va:Fe^{4+}:O^{2-}} - H^{SER}_{Fe} - 3H^{SER}_{O} = 2GPRVOX2 + 1/3GVVV - 4/3GPRVOX1 + GHSEROO + 4.35056T$

$^{\circ}G^{prv}_{Va:Fe^{4+}:Va} - H^{SER}_{Fe} = 2GPRVOX2 + 1/3GVVV - 4/3GPRVOX1 - 2GHSEROO + 4.35056T$

$^{\circ}G^{prv}_{Va:Va:O^{2-}} - 3H^{SER}_{O} = GVVV + 3GHSEROO$

$^{\circ}G^{prv}_{Va:Va:Va} = GVVV$

$p = 0.28 \quad T^{prv}_{c} = 742.88y_{i:j:k} \quad \beta^{prv} = 0.779y_{i:j:k}$

$i = La^{3+}, Va \quad j = Fe^{4+}, \quad Fe^{3+}, Fe^{2+}, Va \quad k = O^{2-}, V$

$LaFe_{12}O_{19}$ hexaferrite (hex)

$(La^{3+})(Fe^{2+})(Fe^{3+})_{11}(O^{2-})_{19}$

$^{\circ}G^{hex}_{La^{3+}:Fe^{2+}:Fe^{3+}:O^{2-}} - H^{SER}_{La} - 12H^{SER}_{Fe} - 19H^{SER}_{O} = GHEX$

Functions

Oxygen

GHSEROO[44]

A-La_2O_3

GLA2O3A[41]

FeO

GWUESTITE[42]

Fe_2O_3

GFE2O3[42]

Orthorhombic perovskite

$GPRV = 0.5GLA2O3A + 0.5GFE2O3 - 65921 + 18.02T - 1.95T \ln T$

$GPRVRED = 0.5GLA2O3A + GWUESTITE + 38,364$

$GPRVOX1 = 0.5GLA2O3A + 3/8GFE2O3 + 3/8GHSEROO - 33,198 + 26.45T$

$GPRVOX2 = 1/3GLA2O3A + 0.5GFE2O3 + 0.5GHSEROO + 5,000$

Rhombohedral perovskite

$GRPRV = 0.5GLA2O3A + 0.5GFE2O3 - 65,563 + 17.74T - 1.95T \ln T$

$GRPRVRED = 0.5GLA2O3A + GWUESTITE + 101,050 - 45.91T$

Orthorhombic and rhombohedral perovskite

GVVV[23]

GL4VO[23]

GLV4O[23]

Hexaferrite

$GHEX = 0.5GLA2O3A + 5.5GFE2O3 + GWUESTITE - 139,562 + 22.63T$

All parameters are in SI units: J, mol, and K

The experimentally determined eutectic compositions and temperatures and the congruent melting temperature of the perovskite phase in the oxide La_2O_3-FeO_x system were reproduced using the temperature-independent regular interaction parameters ${}^0L^{liq}_{Fe^{3+},La^{3+}:O^{2-}} = {}^0L^{liq}_{Fe^{2+},La^{3+}:O^{2-}}$ and subregular interaction parameters ${}^1L^{liq}_{Fe^{3+},La^{3+}:O^{2-}} = {}^1L^{liq}_{Fe^{2+},La^{3+}:O^{2-}}$. It was assumed that the interactions between Fe^{2+}-La^{3+} and Fe^{3+}-La^{3+} are of the same order of magnitude in the oxide melt; thus the two regular interaction parameters were set equal to each other, as were the two subregular interaction parameters. Moruzzi and Shafer[20] explicitly pointed out the uncertainty of the determined eutectic composition at the La-rich side of the system that resulted from limitations of the strip-furnace technique used. So this experiment was given only a little weight during the optimization of interaction parameters of the ionic liquid.

4. Results and Discussion

In Table 2 the Gibbs energy functions and model descriptions of the phases in the La-Fe-O system obtained in this study are listed.

4.1 Oxygen Solubility in Metallic Iron

The reassessed oxygen solubilities in Fe are shown in Fig. 3. The calculated oxygen solubilities in fcc γFe and bcc δFe are in good agreement with the experiments.[47,48]

4.2 La-Fe

The calculated La-Fe phase diagram is presented in Fig. 1, together with the phase diagram data from Gschneidner,[7] Spedding and Daane,[8] Richerd,[9] and Kepka and Skala.[10] The experimentally determined temperatures of the phase transitions are well reproduced by the model.

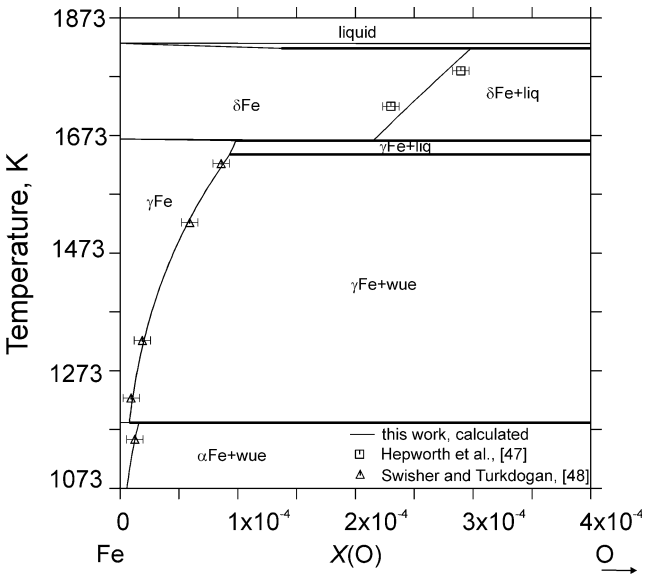

Fig. 3 Calculated oxygen solubilities in Fe with experimental data included (symbols with error bars)

4.2.1 Solid Metals. The positive values of ${}^0L^{bcc}_{Fe,La:Va}$ and ${}^0L^{fcc}_{Fe,La:Va}$ used to model the bcc and fcc phases result in a large miscibility gap between the La-rich and Fe-rich metals. This is tantamount to small mutual solubilities of La and Fe in agreement with the values reported.[7-10] The lack of γLa_{ss} and δFe_{ss} reported by Richerd[9] and the lower melting temperatures of La at 1153 K and Fe at 1807 K compared to the data from Spedding and Daane[8] and Kepka and Skala[10] cannot be reproduced in an equilibrium calculation. However in a calculation excluding bcc, metastable βLa_{ss} is obtained. This phase melts congruently at 1172 K (see Fig. 1), which is 21 K lower than the melting temperature of γLa_{ss}. The Gibbs energy of the transition $\gamma La_{ss} \rightarrow \beta La_{ss}$ is calculated to be 102 J/mol at 1170 K. A calculation of the Gibbs energy of the transition $\delta Fe_{ss} \rightarrow \gamma Fe_{ss}$ gives 59 J/mol at 1773 K, and metastable γFe would melt congruently at 1801 K instead of 1812 K reported for δFe (see Fig. 1). This means that the Gibbs energies of βLa_{ss} and γLa_{ss}, and of γFe_{ss} and δFe_{ss} are rather close to each other, and metastable existence of βLa_{ss} and γFe_{ss} with lower melting points than the stable modifications is conceivable.

4.2.2 Liquid Phase. The calculated enthalpies of mixing of La-Fe liquid are shown in Fig. 4, together with the experimentally determined values.[16,17] If one tries to reproduce the pronounced liquidus anomaly reported (see Fig. 1) by manipulating the interaction parameters of the liquid accordingly, a positive bulge of the enthalpy of mixing illustrated by the dotted line in Fig. 4 is inevitable. This is in disagreement with the experimental mixing

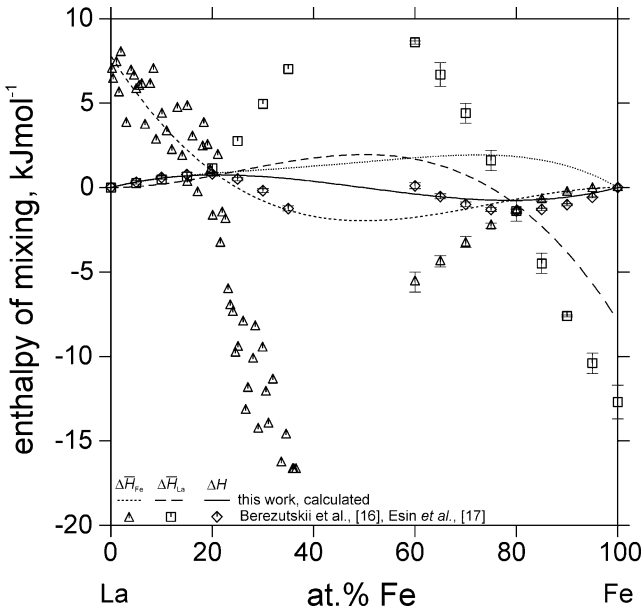

Fig. 4 Calculated partial enthalpies of mixing of La and Fe in La-Fe liquid, and integral enthalpies of mixing as a function of composition, with experiments measured from 0 to 35 at.% Fe at 1723[16] and from 62 to 100 at.% Fe at 1923 K[17] included. Note the obvious deflection of experimentally determined $\Delta\bar{H}_{Fe}$ at 20 at.% Fe. The dotted line represents the calculated integral enthalpy of mixing if the flat liquidus reported in the literature is reproduced

enthalpies from Esin et al.[17] These experiments can only be reproduced by a significantly weaker liquidus anomaly along with a higher Fe content in the liquid at the $\gamma Fe_{ss} \rightarrow \delta Fe_{ss}$ transformation than the proposed value of 75 at.% Fe.[7,8,10] Experimental partial enthalpies of mixing from 0 to 20 at.% Fe[16] and 80 to 100 at.% Fe[17] are fairly well reproduced by the calculation. However, the partial enthalpies from 20 to 70 at.% Fe are in stark contradiction to the phase diagram data: The positive deviations of the liquidus from ideality cannot be accompanied by such a sharp decline of $\Delta\bar{H}_{Fe}$ along with a strong increase of $\Delta\bar{H}_{La}$. The use of these data rules out any reasonable liquidus description; thus they were excluded from the optimization, albeit the cause of this conflict is not clear. As the enthalpies of mixing in the La-Fe melt are rather small, one could at least guess that their precise measurement is particularly challenging. In any case Berezutskii et al.[16] underlined the complexity of thermodynamic experiments in rare earth transition element melts, which is primarily caused by the high reactivity of rare earth elements[1,64] and impurities issues.[64] A better reproduction of the experimental enthalpies of mixing leads to a worse reproduction of the eutectic composition. Even though it is possible to move the latter closer towards the experimental values by a still more positive BT of ${}^{0}L^{liq}_{Fe^{2+},La^{3+}:Va}$ resulting in a higher mixing entropy, this strategy is not recommended, as it inevitably leads to an inverse liquid-liquid miscibility gap, which is definitely unphysical. Actually, the authors could not avoid the appearance of such an inverse miscibility gap at very high temperatures with a minimum at 5180 K and 37 mol.% Fe. Also a metastable liquid-liquid miscibility gap with a maximum at 940 K and 37 at.% Fe results from the presented model.

The liquidus temperatures as determined by Richerd[9] are well reproduced by the model. The optimization of the La-Fe system giving the least square errors between experiments and calculations converged toward the liquidus course shown in Fig. 1 (solid line). It appears that the s-shape of the liquidus resulting from the presented liquid description is a problematic feature, as it contradicts the available phase diagram from the literature.[7-10] However, it is unclear if the reported liquidus curve is drawn based on experiments or assumption. The reproduction of the proposed liquidus curve can be obtained by decreasing BT of ${}^{0}L^{liq}_{Fe^{2+},La^{3+}:Va}$, but this is associated by a eutectic composition with too much Fe. If one tries to move the calculated eutectic composition back to lower Fe contents by increasing A of ${}^{0}L^{liq}_{Fe^{2+},La^{3+}:Va}$, it is clear that the mixing enthalpies become too high. It was not possible to reproduce both enthalpies of mixing and eutectic composition with a "normal" liquidus curve, and the s-shaped liquidus curve is the result of the optimization using available phase diagram and thermodynamic data.

4.3 La-Fe-O

4.3.1 Perovskite Phase. The thermodynamic properties of the $La_{1\pm x}Fe_{1\pm y}O_{3-\delta}$ perovskite phase are well established as several mutually consistent groups of experimental data exist and were obtained by using several different experimental techniques. Only original experimental data were taken for the optimization. In Table 1 thermodynamic standard data of o-$LaFeO_3$ at 298 K are listed that were calculated using this optimized thermodynamic database, together with available data from the literature. We use the enthalpies of formation from the oxides as experimentally determined by Cheng and Navrotsky[26] using drop solution calorimetry in $2PbO{\cdot}B_2O_3$ at 975 K. Enthalpies of formation from the elements[26,30] calculated using enthalpies of formation of the oxides taken from standard compilations were not used for the optimization.

The calculated heat capacities and enthalpy increment data are compared with experiments from the literature in Fig. 5 and 6. These two sets of data were used to optimize the parameter CT ln T of the Gibbs energy of stoichiometric orthorhombic perovskite, ${}^{\circ}G^{o-prv}_{LaFeO_3}$ (GPRV in Table 2). As the Gibbs energy of the stoichiometric perovskite is based on the Gibbs energies of Fe_2O_3 and La_2O_3, this parameter corresponds to a ΔC_P^{o-prv} of formation from the oxides. It is important that the extrapolation of the calculated C_P to high temperatures shows the characteristic smooth flattening above the Dulong-Petit value. Except temperature regions of magnetic or other transitions a negative slope of the C_P function has no physical meaning. Symbols in Fig. 5 represent C_P data of o-$LaFeO_3$ from Stølen et al.[25] A peak with broad shoulders calculated to be present at 740 K is caused by a magnetic order-disorder transition.[25] Two values for the magnetic parameter p are possible depending on the crystal structure, $p = 0.28$ and $p = 0.4$. The C_P anomaly is well reproduced by the model[58,59] using $p = 0.28$. The model was also checked for $p = 0.4$, as the proper p value for structures other than bcc, fcc, and hcp is not available in the literature. The latter optimization resulted in a higher squared error, indicating that a p value of 0.28 is the better choice for orthorhombic perovskite. The averaged deviation of the

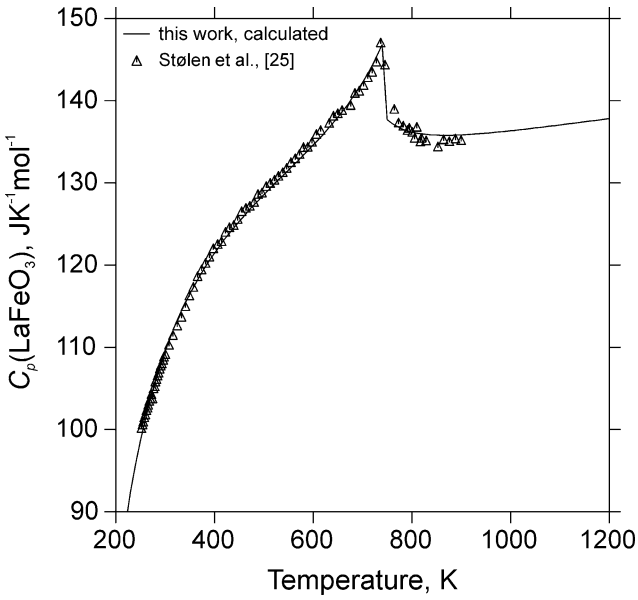

Fig. 5 Calculated heat capacities of $LaFeO_3$ as a function of T with experimental data included (symbols)

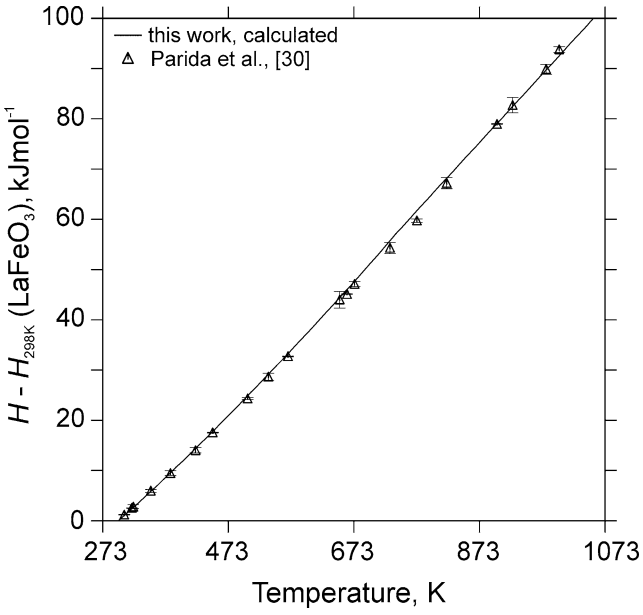

Fig. 6 Calculated enthalpy increments of $LaFeO_3$ as a function of T with experimental data included (symbols). Error bars mark the reported uncertainties

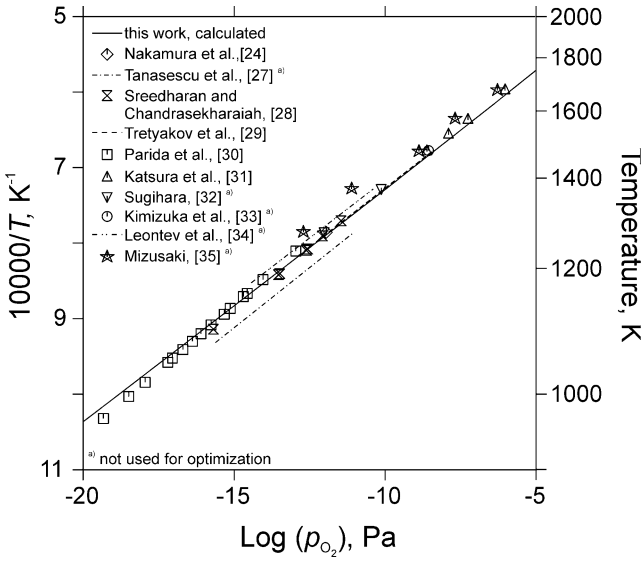

Fig. 7 Assessed Fe-La_2O_3-$La_{1\pm x}Fe_{1\pm y}O_{3-\delta}$ equilibrium logarithmically plotted as a function of p_{O_2} and T (solid line) with experiments included (symbols and broken lines)

calculated heat capacity of o-$LaFeO_3$ from calorimetric results from 250 to 900 K is only 0.55 J/mol K; the maximum deviation, 6.3 J/mol·K, is found in the peak area. The calculated C_P curve extrapolates well to very high temperatures. Enthalpy increment data from Parida et al.[30] were given equal weights as C_P data. The calculated values are very close to the experiments (see Fig. 6). Because of the outstanding consistency between both groups of calorimetric experiments[25,30] the term $CT \ln T$ is fixed firmly.

The emf measurements by Tretyakov et al.[29] were most consistent with the enthalpy of formation as measured by Cheng and Navrotsky[26] (see Fig. 7) and were thus given higher weight in the optimization of the parameters $A + BT$ of the Gibbs energy of the stoichiometric o-perovskite, ${}^{\circ}G^{\text{o-prv}}_{LaFeO_3}$, and its reduced end member, ${}^{\circ}G^{\text{o-prv}}_{LaFeO_{2.5}}$ (GPRV and GPRVRED in Table 2). In general, it can be said that the stability of the perovskite phase has been determined by several groups using several different experimental techniques. Most of these experimental data are very consistent thus putting the thermodynamics of $La_{1\pm x}Fe_{1\pm y}O_{3-\delta}$ on a firm footing.

In Table 1, calculated Gibbs energies of reactions

$$La_2O_3 + Fe + \frac{3}{4}O_{2(g)} \rightarrow LaFeO_3 \qquad \text{(Eq 14)}$$

$$\frac{1}{2}La_2O_3 + \frac{1}{2}Fe_2O_3 \rightarrow LaFeO_3 \qquad \text{(Eq 15)}$$

$$\frac{1}{2}La_2O_3 + \frac{3}{2}FeO \rightarrow \frac{1}{2}Fe + LaFeO_3 \qquad \text{(Eq 16)}$$

are listed together with data from the literature,[24,27-35] which have been corrected by using the assessed Gibbs energies of formation of La_2O_3,[41] and FeO and Fe_2O_3.[42]

Regarding the defect chemistry of the perovskite phase, the defect-reaction for the reduction in $La_{1\pm x}Fe_{1\pm y}O_{3-\delta}$ is written in Eq 17 using the sublattice notation:

$$(La^{3+})(Fe^{3+})(O^{2-})_3 \rightarrow (La^{3+})(Fe^{2+})(O^{2-}_{5/6}Va_{1/6})_3 + \frac{1}{4}O_{2(g)} \uparrow \qquad \text{(Eq 17)}$$

Using the classic defect chemical analysis the proportionalities (in Kröger-Vink notation) $[Fe'_{Fe}] \propto P_{O_2}^{-1/6}$, and $[Va^{\bullet\bullet}_O] \propto P_{O_2}^{-1/6}$ are obtained.[35,39,60]

Equation 18 is the defect reaction for the oxidation in $La_{1\pm x}Fe_{1\pm y}O_{3-\delta}$:

$$2\left[(La^{3+})(Fe^{3+})(O^{2-})_3\right] + \frac{1}{2}O_{2(g)} \rightarrow \left[(La^{3+}_{2/3}, Va_{1/3})(Fe^{4+})(O^{2-})_3\right] + \frac{4}{3}\left[(La_{3+})(Fe^{4+}_{3/4}, Va_{1/4})(O^{2-})_3\right] \qquad \text{(Eq 18)}$$

Using the classic defect chemical analysis the proportionalities (in Kröger-Vink notation) $[Va'''_{La}]$, $[Va'''_{Fe}]$, $[Fe^{\bullet}_{Fe}] \propto P_{O_2}^{3/16}$ are obtained.[39,60]

The dotted lines in Fig. 8 represent the oxygen-nonstoichiometry in cation-stoichiometric lanthanum ferrite calculated using the compound energy formalism considering only reduction of the perovskite phase. The calculated nonstoichiometry fits the experiments best at 1473 K. At 1173 and 1273 K, the calculation deviates significantly from the experimental data. It was tested, if the agreement between calculation and experiments can be improved by introducing interaction parameters into the model. The fit was slightly better at lower temperatures, but this was at the expense of the reproduction of experimental data at 1473 K. Also, as the nonstoichiometries are quite small, very large

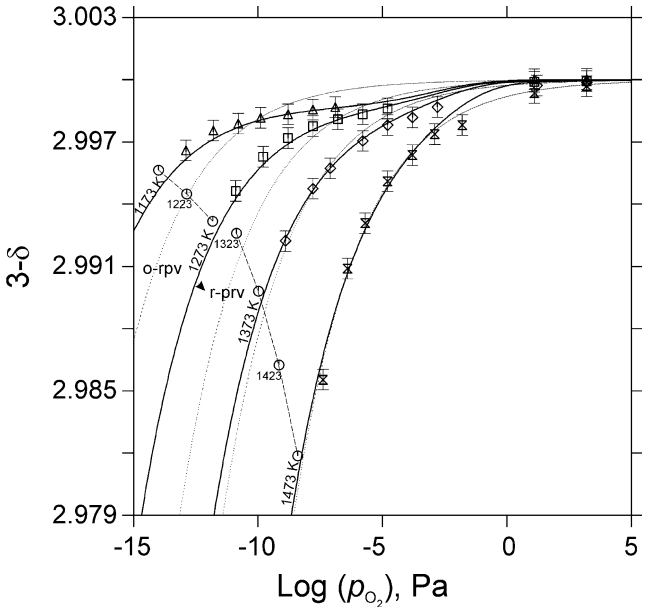

Fig. 8 Oxygen content in $LaFeO_{3-\delta}$ (dotted lines), and in $La_{1\pm x}Fe_{1\pm y}O_{3-\delta}$ with $X(Fe) - X(La) = 0.00018$ (solid lines) as a function of oxygen partial pressures for 1173, 1273, 1373, and 1473 K modeled using the compound energy formalism with experimental data included (symbols with error bars). Dashed lines and circles denote the calculated decomposition of lanthanum ferrite

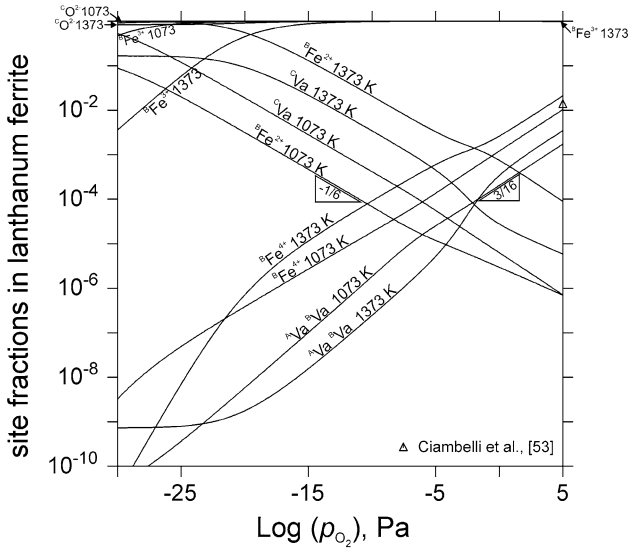

Fig. 9 Calculated site fractions of species in $La_{1\pm x}Fe_{1\pm y}O_{3-\delta}$ logarithmically plotted at 1073 and 1373 K as a function of p_{O_2}. The symbol marks the experimental value of $y^{prv}_{B_{Fe^{4+}}}$ from Ciambelli et al.[53] The slopes of −1/6 and 3/16 of the calculated defect concentrations are indicated in the triangles

interaction parameters were required to change the slope of the curves. Furthermore, the extrapolation to very low oxygen partial pressures was arguable. Other reasons for deviations of experiments from the slope of −1/6 were discussed for the case of $La_{1\pm x}Mn_{1\pm y}O_{3-\delta}$ by Grundy et al.[60] One reason for a change of slope could be defect clustering. However, it is expected that this would lead to a steeper slope, which is opposite to the observed trend. Grundy et al.[57] found that as a result of the disproportionation reaction

$$2Mn^{3+} \rightarrow Mn^{2+} + Mn^{4+} \quad \text{(Eq 19)}$$

defect concentrations changed, again resulting in a steeper slope. In $La_{1\pm x}Fe_{1\pm y}O_{3-\delta}$ the disproportionation reads

$$2Fe^{3+} \rightarrow Fe^{2+} + Fe^{4+} \quad \text{(Eq 20)}$$

In order to account for experimental findings of both small La and Fe deficiencies,[39] and of small amounts of Fe^{4+}[52,53] a sublattice formula with vacancies on the A and B site of lanthanum ferrite, $(La^{3+},Va)(Fe^{2+},Fe^{3+},Fe^{4+},Va)(O^{2-},Va)_3$ is required. Besides, this model allows for disproportionation according to Eq 20. This description leads to a particularly satisfying reproduction of the experimental oxygen-nonstoichiometry data of Mizusaki et al.[38] at low oxygen partial pressures if it is assumed that the perovskites show a slight La deficiency of $X(Fe) - X(La) = 0.00018$ (solid lines in Fig. 9). Mizusaki et al.[38] proposed a similar La deficiency in order to model their experimental data.

Our defect model is also in line with the experimentally determined site fraction of Fe^{4+} from Ciambelli et al.[53] included in Fig. 9. The Fe^{4+} content reported by Porta et al.[52] can only be reproduced in connection with a larger cation solid solubility-range of $La_{1\pm x}Fe_{1\pm y}O_{3-\delta}$, which is not documented. Thus this value was not used for the optimization.

Waernhus et al.[39,40] found that the electrical conductivity of $La_{1\pm x}Fe_{1\pm y}O_{3-\delta}$ at $p_{O_2} > 10$ Pa was time dependent on a time scale of days to weeks. Under these conditions $La_{1\pm x}Fe_{1\pm y}O_{3-\delta}$ is a p-type conductor, with vacancies on the cation sites serving as electron acceptors. It is evident that the larger deviation of the calculation from the experiments at high oxygen partial pressures—even though it is within the margin of errors reported—is caused by nonequilibrium conditions of the thermogravimetric experiments because of insufficient reaction times, namely 10 min for each experiment.[38] The measurements were conducted by reducing the perovskite phase at a very low oxygen partial pressure and then flushing the furnace with oxygen, thereby provoking the formation of cation vacancies during gradually increasing oxygen partial pressure. The weight increase of the perovskite phase because of its oxidation was monitored as a function of the increase in oxygen partial pressure. The formation of cation vacancies involves cation diffusion, which is a slow process.[39,40] At $p_{O_2} > 10$ Pa the reaction time was most likely too short for the perovskite phase to reach equilibrium with the atmosphere. Consequently these experiments were excluded from the optimization.

The dashed lines in Fig. 8 show the calculated oxygen partial pressures of the decomposition of $La_{1\pm x}Fe_{1\pm y}O_{3-\delta}$. The following oxygen nonstoichiometries of this single-phase perovskite were calculated at its decomposition:

$\delta = 0.0044$ at $p_{O_2} = 10^{-14}$ Pa and $T = 1173$ K, and $\delta = 0.018$ at $p_{O_2} = 10^{-8.4}$ and $T = 1473$ K. The concentrations of the defects $Fe_{Fe}^{\bullet}$, Fe_{Fe}^{x}, $Fe_{Fe}^{\prime}$, La_{La}^{x}, $[Va_{La}^{\prime\prime\prime}]$, $[Va_{Fe}^{\prime\prime\prime}]$, O_O^x and $Va_O^{\bullet\bullet}$ in $La_{1\pm x}Fe_{1\pm y}O_{3-\delta}$ correspond to the site fractions $y_{B Fe^{4+}}^{prv}$, $y_{B Fe^{3+}}^{prv}$, $y_{B Fe^{2+}}^{prv}$, $y_{A_{La^{3+}}}^{prv}$, $y_{A Va}^{prv}$, $y_{B Va}^{prv}$, $y_{C O^{2-}}^{prv}$, and $y_{C Va}^{prv}$ in the compound energy formalism. These are plotted logarithmically as a function of $\log p_{O_2}$ at 1073 and 1373 K in Fig. 9 for $La_{1\pm x}Fe_{1\pm y}O_{3-\delta}$ with $x = y$, together with the experiment from Ciambelli et al.[53] The slopes of −1/6 and 3/16 of the defect concentrations shown in the triangles are fixed by the defect reactions Eq 17 and 18. These are reproduced by the calculated slopes using the compound energy formalism from $p_{O_2} \approx 10^{-15}$ to 10^{-7} Pa, and $p_{O_2} \approx 10$ to 10^5 Pa, respectively. This means that the defect chemistry of lanthanum ferrite is governed by reduction from $p_{O_2} \approx 10^{-15}$ to 10^{-7} Pa, and by oxidation from $p_{O_2} \approx 10$ to 10^5 Pa. For cation stoichiometric $La_{1\pm x}Fe_{1\pm y}O_{3-\delta}$ $[Va_{Fe}^{\prime\prime\prime}]$ equals $[Va_{La}^{\prime\prime\prime}]$ in our model, in line with Waernhus et al.[40] $[Va_{Fe}^{\prime\prime\prime}]$ and $[Va_{La}^{\prime\prime\prime}]$ are markedly dependent on the oxygen partial pressure, while the influence of temperature is less pronounced. On the other hand Mizusaki et al.[35] stated that $[Va_{Fe}^{\prime\prime\prime}]$ would be negligible, and $[Va_{La}^{\prime\prime\prime}]$ would be the electron acceptor, based on the assumption that the BO_3 portion of ABO_3 in perovskite is stoichiometric, whereas the A site may easily be deficient. This contradicts the experimental findings of small amounts of excess La^{3+} in single-phase lanthanum ferrite,[39] and Fe^{4+} identified in cation stoichiometric $LaFeO_{3-\delta}$.[52,53] In their defect model, $[Va_{La}^{\prime\prime\prime}]$ does not depend on the oxygen partial pressure, whereas in our model the number of acceptors decreases with decreasing p_{O_2}. In lanthanum manganite large charge disproportionation causes a steeper slope of the defect concentrations as a function of p_{O_2},[60] whereas the calculated charge disproportionation in lanthanum ferrite is too small to affect the defect chemistry of the perovskite phase to a comparable extent: Cation stoichiometric $LaFeO_{3-\delta}$ contains only 0.009% Fe^{2+} and Fe^{4+} at 1073 K, and 0.14% Fe^{2+} and Fe^{4+} at 1373 K.

It is quite evident from Fig. 9 that the new defect model of $La_{1\pm x}Fe_{1\pm y}O_{3-\delta}$ using the compound energy formalism extrapolates well to very low oxygen partial pressures. Moreover, the presented description optimized by experiments is consistent with the classic defect chemistry analysis.

4.3.2 Hexaferrite Phase. The Gibbs energy of $LaFe_{12}O_{19}$ hexaferrite was optimized on the basis of its stability range in the phase diagram because no measurements of its thermodynamic properties exist. The formation of $LaFe_{12}O_{19}$ from La_2O_3 and Fe_2O_3 reads:

$$\frac{1}{2}La_2O_3 + 6Fe_2O_3 \rightarrow LaFe_{12}O_{19} + \frac{1}{4}O_{2(g)} \uparrow \qquad \text{(Eq 21)}$$

and the Gibbs energy of formation from La_2O_3 and Fe_2O_3, $\Delta_{f,oxides}\,{}^{\circ}G(LaFe_{12}O_{19})$ is calculated:

$$\Delta_{f,oxides\ (1073-1723\,K)}\,{}^{\circ}G(LaFe_{12}O_{19}) = 4634 - 37.071T \quad \text{(J/mol)} \qquad \text{(Eq 22)}$$

For the standard enthalpy of formation from the elements the authors get $\Delta_{f,elements}{}^{\circ}H_{298\,K} = -5745$ kJ/mol. The standard entropy yields ${}^{\circ}S_{298\ K} = 683$ J/mol·K. Experimental thermodynamic data of $SrFe_{12}O_{19}$, which is isostructural with $LaFe_{12}O_{19}$ and also contains a large cation, Sr^{2+}, were assessed in the Sr-Fe-O system.[65] Resulting calculated thermodynamic standard data for $SrFe_{12}O_{19}$ are $\Delta_f\,{}^{\circ}H_{298\,K} = -5545$ kJ/mol, and ${}^{\circ}S_{298\,K} = 633$ J/mol·K. $SrFe_{12}O_{19}$ can be formed from the oxides by the reaction

$$SrO + 6Fe_2O_3 \rightarrow SrFe_{12}O_{19} \qquad \text{(Eq 23)}$$

The calculated thermodynamic data of $LaFe_{12}O_{19}$ and $SrFe_{12}O_{19}$ lie in a comparable range. As both phases have the same structure, and ionic radii are similar, these results indicate that the presented thermodynamic data of $LaFe_{12}O_{19}$—even though they are rather tentative—are very reasonable.

4.4 Phase Diagrams

4.4.1 $LaO_{1.5}$-FeO_x. The calculated $LaO_{1.5}$-FeO_x phase diagram in air atmosphere is presented in Fig. 2 (solid lines) together with data from Moruzzi and Shafer[20] (broken lines and symbols). Though small deviations of the calculated temperature range of stable $Fe_{3-x}O_4$ from the phase diagram data of Moruzzi and Shafer[20] exist, we decided not to change its description adopted from Selleby and Sundman.[42] $LaO_{1.5}$-FeO_x phase diagrams in pure oxygen at $p_{O_2} = 10^5$ Pa, in air at $p_{O_2} = 21278$ Pa, and under reducing conditions at $p_{O_2} = 0.01$ Pa are presented in Fig. 10(a) to (c).

r-$La_{1\pm x}Fe_{1\pm y}O_{3-\delta}$ melts at 2176 K at $p_{O_2} = 10^5$ Pa; 2136 K is calculated in air. At $p_{O_2} = 0.01$ Pa (Fig. 10c), the temperature of the transition o-prv → r-prv is 1283 K, 4 K higher than in air and pure oxygen. Under these reducing conditions, $LaFe_{12}O_{19}$ is stable from $T = 957$ to 1247 K. At $p_{O_2} = 10^5$ Pa (Fig. 10a) $LaFe_{12}O_{19}$ is not stable.

The calculated eutectic at the $LaO_{1.5}$-rich side changes from $T = 2055$ K and 32.0 cat.% Fe in air (Fig. 10b) to 2077 K and 30.9 cat.% in pure oxygen; for the eutectic at the Fe-rich side $T = 1704$ K and 88.8 cat.% Fe in pure oxygen, and 1701 K and 88.5 cat.% Fe in air are calculated. Fe^{3+} in the liquid is favored over Fe^{2+} under oxidizing conditions. The oxidation of Fe^{2+} to Fe^{3+} in the liquid governs shifts of eutectic compositions and temperatures and of the melting temperature of the perovskite phase on increasing the oxygen partial pressure. At $p_{O_2} = 0.01$ Pa (Fig. 10c), a significant amount of Fe^{3+} in the ionic liquid is reduced to Fe^{2+}, and the liquid stability increases considerably at the Fe-rich part of the system leading to a strongly lowered eutectic temperature. Oxide liquid first forms by the simplified eutectic reaction

$$Fe_{3-x}O_4 + \text{r-}La_{1\pm x}Fe_{1\pm y}O_{3-\delta} \rightarrow \text{liquid} \qquad \text{(Eq 24)}$$

at 1573 K and 85.4 cat.% Fe. r-$La_{1\pm x}Fe_{1\pm y}O_{3-\delta}$ melts congruently at 1777 K.

A calculated isothermal section of the La_2O_3-FeO-FeO_2 oxide system at 1273 K is shown in Fig. 11. Lanthanum

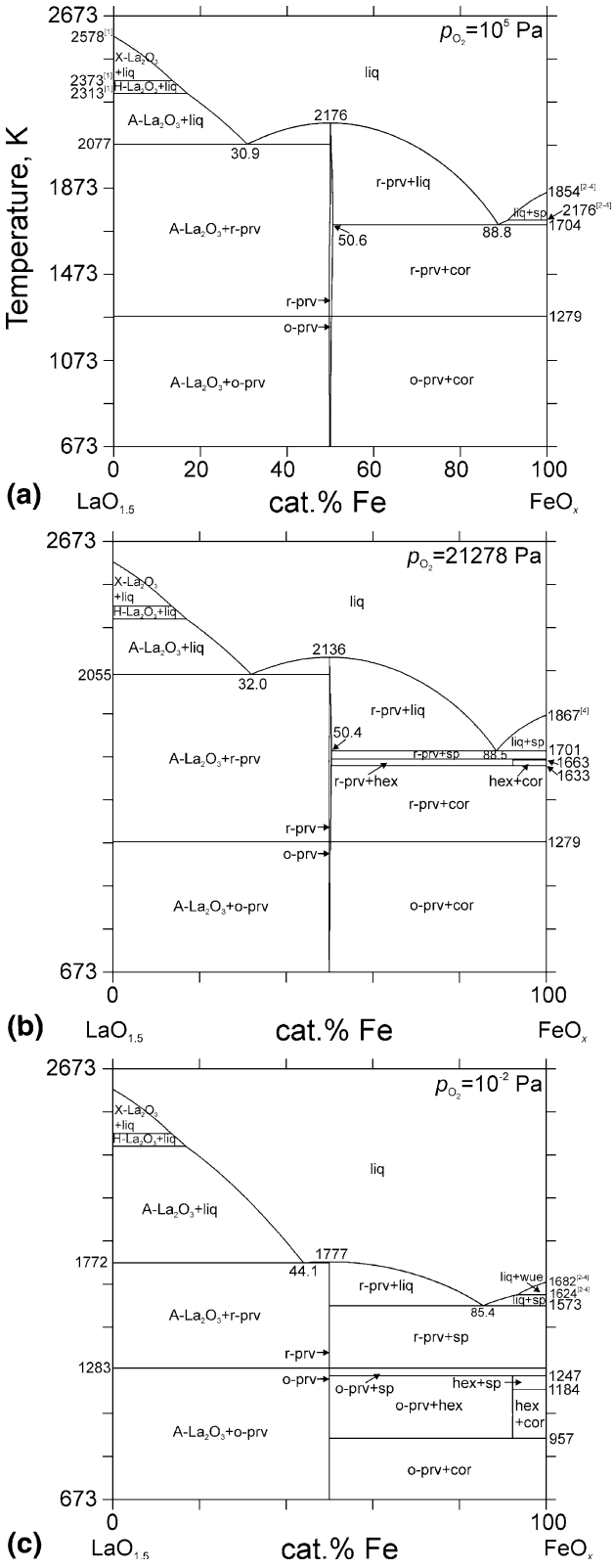

Fig. 10 Calculated phase diagrams of the $LaO_{1.5}$-FeO_x system in pure oxygen (a), air atmosphere (b), and under reducing conditions at $p_{O_2} = 0.01$ Pa (c)

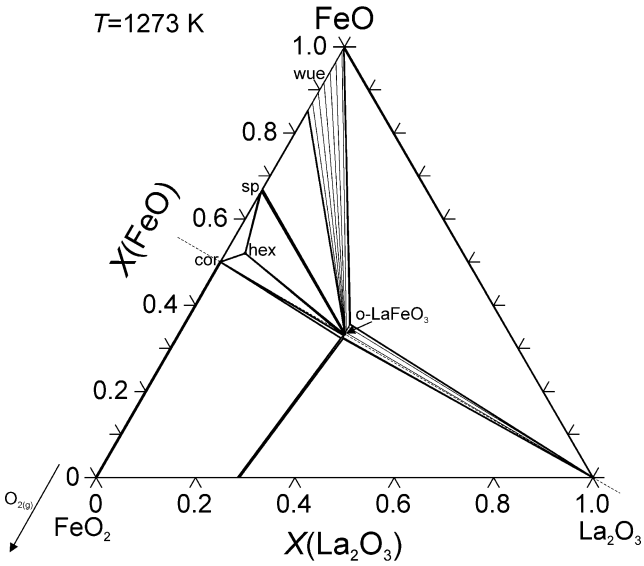

Fig. 11 Calculated isothermal section of the La_2O_3-FeO-FeO_2 oxide system at 1273 K representing oxide phase equilibria. The dashed line marks the quasi-binary $LaO_{1.5}$-$FeO_{1.5}$ section

ferrite with slight cation-nonstoichiometry can be in equilibrium with La_2O_3, Fe_2O_3, or $O_{2(g)}$, whereas $Fe_{1-\delta}O$ can be in equilibrium with cation stoichiometric perovskite only.

4.4.2 La-Fe-O. In Fig. 12(a) to (c) calculated phase equilibria of the La-Fe-O system at 873, 1073, and 1273 K are shown as a function of oxygen partial pressures. With increasing temperature A-La_2O_3 + Fe, o-prv + Fe, and o-prv + $Fe_{1-x}O$ are stable in a larger p_{O_2} range, opposite to the other subsolidus phase equilibria. La is not dissolved in Fe down to $p_{O_2} = 10^{-33}$ Pa at $T \leq 1273$ K. Cation stoichiometry in the perovskite phase increases with increasing oxygen partial pressure. Liquid formation is restricted to oxygen partial pressures $< 10^{-34}$ Pa at $T \leq 1273$ K.

5. Conclusions

The presented thermodynamic database of the La-Fe-O system is consistent with most of the thermodynamic and phase diagram experiments. The presented s-shaped liquidus curve of the metallic liquid deviating from the suggested liquidus curve from the literature results from the optimization of model parameters by using both phase diagram and thermodynamic data, and the existence of a liquid-liquid miscibility gap in the La-Fe subsystem can be ruled out. Thermodynamic standard data of $LaFe_{12}O_{19}$ are presented for the first time. The magnetic order-disorder transition and the orthorhombic-rhombohedral phase transition in lanthanum ferrite are well reproduced by the model. The modeling of nonstoichiometries in $La_{1\pm x}Fe_{1\pm y}O_{3-\delta}$ can be used to calculate its defect chemistry under varying temperature and oxygen partial pressure conditions. Defect chemistry,

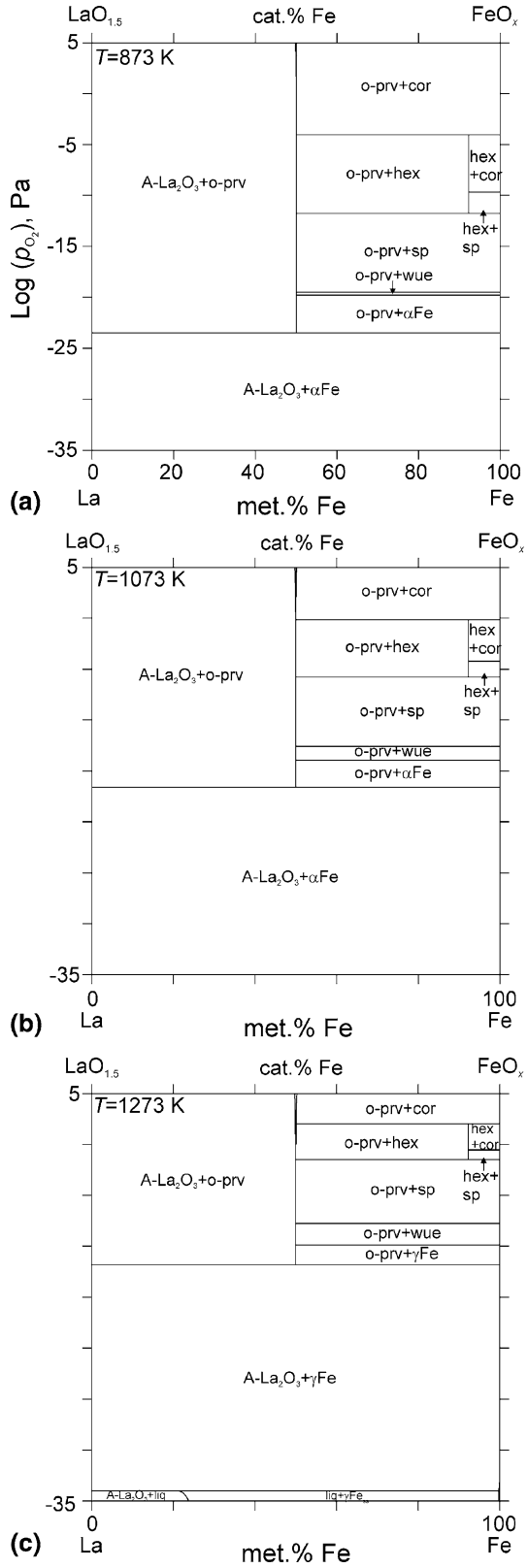

Fig. 12 Calculated phase equilibria of the La-Fe-O system at 873 K (a), 1073 K (b), and 1273 K (c) as a function of oxygen partial pressure

magnetic behavior, and phase transition of the perovskite phase have to be considered in the modeling of doped lanthanum ferrite, as they are most likely of significance for the electrochemical performance of high- to intermediate-temperature solid oxide fuel cells operated with LSCF cathodes.

Acknowledgment

This work was financially supported by the Federal Agency for Education and Science, Sixth Framework Program for Research and Technical Development of the European Union.

References

1. L.V. Goncharuk and V.R. Sidorko, Thermodynamics of Interaction of Rare-Earth Metals with *d*-Metals. The Scandium—Iron System, *Powder Metall. Met. Ceram.*, 2001, **40**(7-8), p 354-361
2. E.M. Savitskii, Investigation of the Physico-Chemical Interactions of Rare-Earth Metals with Iron and Steel, *Proc. Conf. Rare Earth Elements for Steel and Alloys*, 1959, p 31-49
3. J. Linden, "Austenitic Stainless Steel with High Oxidation Resistance," Patent DE69813156T2 06.11.2003, EP-number: 0921206. www.patent-de.com/20031106/DE69813156T2.html
4. M. Küpferling, V.C. Flores, R. Grössinger, and M. Aquino, Preparation and Characterization of $LaFe_{12}O_{19}$ Hexaferrite, *J. Magn. Magn. Mater.*, 2005, **290-291**, p 1255-1258
5. A.M. Van Diepen and F.K. Lotgering, Mössbauer Effect in $LaFe_{12}O_{19}$, *J. Phys. Chem. Solids*, 1974, **35**, p 1641-1643
6. E. Pollert, Crystal Chemistry of Magnetic Oxides Part 2: Hexagonal Ferrites, *Prog. Cryst. Growth Charact.*, 1985, **11**, p 155-205
7. K.A. Gschneidner, Jr., *Rare Earth Alloys, A Critical Review of the Alloy Systems of the Rare Earth, Scandium and Yttrium Metals*, D. Van Nostrand Company, Princeton, NJ, 1961, p 187-188
8. F.H. Spedding and A.H. Daane, Ed., *The Rare Earths*, John Wiley & Sons, New York, 1961, p 280, 415-416
9. J. Richerd, Lanthanum and Cerium in Pure Iron, *Mem. Sci. Rev. Metall.*, 1962, **59**(7-8), p 539-548, in French
10. M. Kepka and J. Skala, Effect of Rare-Earth Elements on Properties of Steels, *Hutník*, 1972, **22**(1), p 12-17, in Czech
11. K. Nassau, L.V. Cherry, and W.E. Wallace, Intermetallic Compounds between Lanthanons and Transition Metals of the First Long Period. I—Preparation, Existence and Structural Studies, *J. Phys. Chem. Solids*, 1960, **16**, p 123-130
12. J.F. Cannon, D.L. Robertson, and H.T. Hall, Synthesis of Lanthanide-Iron Laves Phases at High Pressures and Temperatures, *Mater. Res. Bull.*, 1972, **7**, p 5-12
13. E.M. Savitskii, *Rare Metals and Alloys,* Dom Tekhniki, Moscow, 1959, in Russian. Cited by Ref 11
14. E.M. Savitskii, Rare-Earth Metals, *Metalloved. Term. Obrab. Met.*, 1961, **9**, p 28, in Russian
15. W. Zhang and C. Li, The Fe-La (Iron-Lanthanum) System, *J. Phase Equilib.*, 1997, **18**(3), p 301-304
16. V.V. Berezutskii, N.I. Usenko, and M.I. Ivanov, Thermochemistry of Binary Alloys of Lanthanum with 3*d*-Transition Metals, *Powder Metall. Met. Ceram.*, 2006, **45**(5-6), p 266-271
17. Y.O. Esin, A.F. Ermakov, M.G. Valishev, G.M. Ryss, P.V. Geld, and E.S. Levin, Enthalpy of Formation of Liquid Binary

Alloys of Iron with Lanthanum and Cerium, *Zh. Fiz. Khim.*, 1981, **55**(7), p 1665-1669, in Russian
18. H. Okamoto, Thermodynamically Improbable Phase Diagrams, *J Phase Equilib.*, 1991, **12**(2), p 148-168
19. H. Okamoto, *Phase Diagrams of Binary Iron Alloys*, ASM International, Materials Park, OH, 1993, p 341-349
20. V.L. Moruzzi and M.W. Shafer, Phase Equilibria in the System La_2O_3-Iron Oxide in Air, *J. Am. Ceram. Soc.*, 1960, **43**(7), p 367-372
21. J. Cassedanne and H. Forestier, Investigation of the Systems Fe_2O_3-La_2O_3 and Fe_2O_3-Sc_2O_3, *C. R. Acad. Sci. (Paris)*, 1960, **250**, p 2898-2900, in French
22. M. Kowalski and P.J. Spencer, Thermodynamic Reevaluation of the Cr-O, Fe-O and Ni-O Systems: Remodelling of the Liquid, BCC and FCC Phases, *Calphad*, 1995, **19**(3), p 229-243
23. A.N. Grundy, B. Hallstedt, and L.J. Gauckler, Thermodynamic Assessment of the Lanthanum-Oxygen System, *J. Phase Equilib.*, 2001, **22**(2), p 105-113
24. T. Nakamura, G. Petzow, and L.J. Gauckler, Stability of the Perovskite Phase $LaBO_3$ (B = V, Cr, Mn, Fe, Co, Ni) in Reducing Atmosphere I. Experimental Results, *Mater. Res. Bull.*, 1979, **14**, p 649-659
25. S. Stølen, F. Grønvold, H. Brinks, T. Atake, and H. Mori, Heat Capacity and Thermodynamic Properties of $LaFeO_3$ and $LaCoO_3$ from T = 13 K to T = 1000 K, *J. Chem. Thermodyn.*, 1998, **30**, p 365-377
26. J. Cheng and A. Navrotsky, Enthalpies of Formation of $LaMO_3$ Perovskites (M = Cr, Fe, Co, and Ni), *J. Mater. Res.*, 2005, **20**(1), p 191-200
27. S. Tanasescu, N.D. Totir, and D.I. Marchidan, Thermodynamic Properties of $LaFeO_3$ Studied by Means of Galvanic Cells with Solid Oxide Electrolyte, *Mater. Res. Bull.*, 1997, **32**(7), p 925-931
28. O.M. Sreedharan and M.S. Chandrasekharaiah, Standard Gibbs' Energy of Formation of $LaFeO_3$ and Comparison of Stability of $LaMO_3$ (M = Mn, Fe, Co or Ni) Compounds, *J. Mater. Sci.*, 1986, **21**, p 2581-2584
29. Y.D. Tretyakov, A.R. Kaul, and V.K. Portnoy, Formation of Rare Earth and Yttrium Orthoferrites: A Thermodynamic Study, *High Temp. Sci.*, 1977, **9**, p 61-70
30. S.C. Parida, Z. Singh, S. Dash, R. Prasad, and V. Venugopal, Thermodynamic Studies on $LaFeO_3$(s), *J. Alloys Compd.*, 1998, **280**, p 94-98
31. T. Katsura, T. Sekine, K. Kitayama, and T. Sugihara, Thermodynamic Properties of Fe-Lanthanoid-O Compounds at High Temperatures, *J. Solid State Chem.*, 1978, **23**, p 43-57
32. T. Sugihara, Thesis of D.Sc., Department of Chemistry, Faculty of Science, Tokyo Institute of Technology, Meguro-ku, Tokyo, Japan, 1979, p 152, in Japanese
33. N. Kimizuka and T. Katsura, The Standard Free Energy of the Formation of $LaFeO_3$ at 1204°C, *Bull. Chem. Soc. Jpn.*, 1974, **47**(7), p 1801-1802
34. S.A. Leontev, Y.P. Vorobev, A.M. Balbechor, A.N. Men, A.Y. Cherronenkis, and G.I. Chufaov, Thermodynamic Properties of Orthoferrites of Rare-Earth Elements and Yttrium, *Dokl. Akad. Nauk USSR*, 1973, **209**, p 618-620, in Russian
35. J. Mizusaki, T. Sasamoto, W.R. Cannon, and H.K. Bowen, Electronic Conductivity, Seebeck Coefficient, and Defect Structure of $LaFeO_3$, *J. Am. Ceram. Soc.*, 1982, **65**(8), p 363-368
36. A. Fossdal, M. Menon, I. Waernhus, K. Wiik, M.-A. Einarsrud, and T. Grande, Crystal Structure and Thermal Expansion of $La_{1-x}Sr_xFeO_{3-\delta}$ Materials, *J. Am. Ceram. Soc.*, 2004, **87**(10), p 1952-1958
37. S. Geller and P.M. Raccah, Phase Transitions in Perovskitelike Compounds of the Rare Earths, *Phys. Rev. B*, 1970, **2**(4), p 1167-1172
38. J. Mizusaki, M. Yoshihiro, S. Yamauchi, and K. Fueki, Nonstoichiometry and Defect Structure of the Perovskite-Type Oxides $La_{1-x}Sr_xFeO_{3-\delta}$, *J. Solid State Chem.*, 1985, **58**, p 257-266
39. I. Waernhus, P.E. Vullum, R. Holmestad, T. Grande, and K. Wiik, Electronic Properties of Polycrystalline $LaFeO_3$. Part I: Experimental Results and the Qualitative Role of Schottky Defects, *Solid State Ionics*, 2005, **176**, p 2783-2790
40. I. Waernhus, T. Grande, and K. Wiik, Electronic Properties of Polycrystalline $LaFeO_3$. Part II: Defect Modelling Including Schottky Defects, *Solid State Ionics*, 2005, **176**(35-36), p 2609-2616
41. M. Zinkevich, S. Geupel, F. Aldinger, A. Durygin, S.K. Saxena, M. Yang, and Z.-K. Liu, Phase Diagram and Thermodynamics of the La_2O_3-Ga_2O_3 System Revisited, *J. Phys. Chem. Solids*, 2006, **67**, p 1901-1907
42. M. Selleby and B. Sundman, A Reassessment of the Ca-Fe-O System, *Calphad*, 1996, **20**(3), p 381-392
43. J.R. Taylor and A.T. Dinsdale, A Thermodynamic Assessment of the Cr-Fe-O System, *Z. Metallkd.*, 1993, **84**, p 335-345
44. A.T. Dinsdale, SGTE Data for Pure Elements, *Calphad*, 1991, **15**(4), p 317-425
45. B. Hallstedt, N. Dupin, M. Hillert, L. Höglund, H.L. Lukas, J.C. Schuster, and N. Solak, Thermodynamic Models for Crystalline Phases. Composition Dependent Models for Volume, Bulk Modulus and Thermal Expansion, *Calphad*, 2007, **31**(1), p 28-37
46. B. Sundman, B. Jansson, and J.-O. Andersson, The Thermo-Calc Databank System, *Calphad*, 1985, **9**(2), p 153-190
47. M.T. Hepworth, R.P. Smith, and E.T. Turkdogan, Permeability Solubility and Diffusivity of Oxygen in Bcc Iron, *Trans. AIME*, 1966, **236**, p 1278
48. J.H. Swisher and E.T. Turkdogan, Solubility Permeability and Diffusivity of Oxygen in Solid Iron, *Trans. AIME*, 1967, **239**, p 426-431
49. M. Chen, B. Hallstedt, and L.J. Gauckler, Thermodynamic Assessment of the Co-O System, *J. Phase Equilib.*, 2003, **24**(3), p 212-227
50. N. Saunders and A.P. Miodownik, *Calphad Calculation of Phase Diagrams,* Pergamon Materials Series, Vol 1. Elsevier Science Ltd., Oxford, UK, 1998, p 94-96
51. B.C. Tofield and W.R. Scott, Oxidative Nonstoichiometry in Perovskite, an Experimental Survey; the Defect Structure of an Oxidized Lanthanum Manganite by Powder Neutron Diffraction, *J. Solid State Chem.*, 1974, **10**, p 183-194
52. P. Porta, S. Cimino, S. De Rossi, M. Faticanti, G. Minelli, and I. Pettiti, $AFeO_3$ (A = La, Nd, Sm) and $LaFe_{1-x}Mg_xO_3$ Perovskites: Structural and Redox Properties, *Mater. Chem. Phys.*, 2001, **71**, p 165-173
53. P. Ciambelli, S. Cimino, S. De Rossi, L. Lisi, G. Minelli, P. Porta, and G. Russo, $AFeO_3$ (A = La, Nd, Sm) and $LaFe_{1-x}Mg_xO_3$ Perovskites as Methane Combustion and CO Oxidation Catalysts: Structural, Redox and Catalytic Properties, *Appl. Catal. B Environ.*, 2001, **29**, p 239-250
54. J.-O. Andersson, A.F. Guillermet, M. Hillert, B. Jansson, and B. Sundman, A Compound-Energy Model of Ordering in a Phase with Sites of Different Coordination Numbers, *Acta Metall.*, 1986, **34**, p 437-445
55. M. Hillert, B. Jansson, and B. Sundman, Application of the Compound-Energy Model to Oxide Systems, *Z. Metallkd.*, 1988, **79**(2), p 81-87

56. M. Hillert, The Compound Energy Formalism, *J. Alloys Compd.*, 2001, **320**, p 161-176
57. A.N. Grundy, M. Chen, B. Hallstedt, and L.J. Gauckler, Assessment of the La-Mn-O System, *J. Phase Equilib. Diff.*, 2005, **26**(2), p 131-151
58. G. Inden, Determination of Chemical and Magnetic Interchange Energies in BCC Alloys. I. General Treatment, *Z. Metallkd.*, 1975, **66**(10), p 577-582
59. M. Hillert and M. Jarl, A Model of Alloying Effects in Ferromagnetic Metals, *Calphad*, 1978, **2**(3), p 227-238
60. A.N. Grundy, E. Povoden, T. Ivas, and L.J. Gauckler, Calculation of Defect Chemistry Using the CALPHAD Approach, *Calphad*, 2005, **30**, p 33-41
61. A. Deschamps and F. Bertaut, On the Substitution of Al, Ga, and Cr with Fe in Baryum Hexaferrite $BaO.6Fe_2O_3$, *C. R. Acad. Sci. (Paris)*, 1957, **244**, p 3069-3072, in French
62. M. Hillert, B. Jansson, B. Sundman, and J. Ågren, A Two-Sublattice Model of Molten Solutions with Different Tendency of Ionization, *Metall. Trans. A*, 1985, **16A**, p 261-266
63. B. Sundman, Modification of the Two-Sublattice Model for Liquids, *Calphad*, 1991, **15**, p 109-119
64. R. Ferro, G. Borzone, G. Cacciamani, and N. Parodi, Thermodynamics of Rare Earth Alloys: Systematics and Experimental, *Themochim. Acta*, 1998, **314**(1-2), p 183-204
65. E. Povoden, A.N. Grundy, M. Chen, T. Ivas and L.J. Gauckler, Thermodynamic Assessment of the La-Sr-Fe-O System, in preparation